Analysis and stability of modern power systems using high fidelity modeling

Gabriel Colon-Reyes

Electrical Engineering and Computer Sciences
University of California, Berkeley

Technical Report No. UCB/EECS-2025-154
http://www2.eecs.berkeley.edu/Pubs/TechRpts/2025/EECS-2025-154.html

August 13, 2025

Analysis and stability of modern power systems using high fidelity modeling

by

Gabriel E. Colón Reyes

A dissertation submitted in partial satisfaction of the

requirements for the degree of

Doctor of Philosophy

in

Electrical Engineering and Computer Sciences

in the

Graduate Division

of the

University of California, Berkeley

Committee in charge:

Professor Duncan S. Callaway, Co-chair
Professor Claire J. Tomlin, Co-chair
Assistant Professor Jessica Boles

Summer 2025

Analysis and stability of modern power systems using high fidelity modeling

Abstract

Analysis and stability of modern power systems using high fidelity modeling

by

Gabriel E. Colón Reyes

Doctor of Philosophy in Electrical Engineering and Computer Sciences

University of California, Berkeley

Professor Duncan S. Callaway, Co-chair

Professor Claire J. Tomlin, Co-chair

Modern power systems are undergoing large changes in their physical behavior. Fossil fuel-based generation is rapidly being replaced by renewable and storage energy sources, which are connected to the grid via power electronic devices called converters. These devices behave drastically different than synchronous generators powered by fossil fuels. Further, with trends in electrification, many new devices at the electricity consumer level are also in the form of power electronics. The combination of these two trends has meant that many new devices that have not been previously studied in detail in a power systems context are making their way onto the grid.

This thesis addresses questions that enhance our understanding of grid behavior when these new power electronics devices are being interconnected. In particular, we use different modeling approaches at the different power system levels, i.e., generation, transmission, and load, to draw conclusions on how the incorporation of these devices affect power system behaviors.

On the generation level, we model converters using a hybrid systems modeling approach and arrive at the first globally asymptotically stabilizing switching control law for sinusoidal reference tracking of inverters. At the transmission level, we model transmission lines with different degrees of fidelity showing that the standard π topology modeled with differential equations is a suitable model to use when performing both small signal and dynamic simulation analyses of power systems. At the load level, we propose ZIP-E loads, a new modeling framework which builds on the industry standard ZIP load to capture the dynamic behavior introduced by power electronic loads. We find that when using load models that capture power electronic loads' dynamic behavior small signal stability holds for a larger and heavier range of network loading conditions. We also find that transient responses are generally more damped for systems with dynamic power electronic load models. Lastly, we study *abc*- and *dq*-frame modeling for power systems. In particular, due to a lack of clarity in the literature,

we derive precise relationships between signals in the different reference frames that allow us to make specific one-to-one conclusions between results in *abc* and *dq* frames. This allows us to precisely use *dq* models to arrive at *abc* conclusions.

A mi familia

Arnaldo, Jossie y Kamila. And to those who over time became my family too.

Contents

List of Figures

List of Tables

Acknowledgments

The PhD journey can be a lonely one at many times, unfortunately. However, at the end it is clear that I had many people at my side throughout making the experience significantly better, and that's worth recognizing.

I would like to first acknowledge and thank my research advisors Duncan Callaway and Claire Tomlin. Duncan has been a consistent supporter of my work, always pushing me to understand why we are pursuing the questions we are exploring, and encouraged me in pursuing my research ideas while also making sure we stay centered in our objective. Duncan's questions and continuous challenge of my research ideas forced me think outside of my comfort zone allowing me to arrive at conclusions that would not have been possible on my own. Our meeting times were extremely valuable making tremendous headway through brainstorming and discussion and I appreciate his time spent on that. Claire has also been instrumental in my journey. She has been a consistent source of support and always encouraged me to ensure that the research I pursued was not only theoretically important, but that was also of real practical value. Her guidance, mentorship, and commitment to her students' success was particularly relevant for my PhD, and I appreciate that greatly.

I would also like to acknowledge other professors who contributed to my PhD in different ways beginning with Jessica Boles for taking on the role of my qualifying exam chair, and being on my thesis committee. I would also like to acknowledge professor Bri-Mathias Hodge (CU Boulder) for participating in my qualifying exam committee. Lastly, I want to thank my first PhD advisor Sascha von Meier because she offered me the opportunity to come to UC Berkeley as a graduate student and for that I am grateful.

In addition to working with professors, I had the great opportunity to work closely with fellow students who later became great colleagues and friends. In particular, I would like to acknowledge Ruth Kravis, Sunash Sharma, Kaylene Stocking, and Reid Dye for their support and interest in my research which led to direct contributions to this thesis, and publishing research articles together. I would also like to acknowledge PhD friends and colleagues Mohini Bariya, Keith Moffat, Jaimie Swartz, Miles Rusch, Sara Pohland, Jason Choi, Jingqi Li, Victoria Tuck, Liyang Wang, Eli Brock, among others that I surely missed but also made my PhD experience better.

I would also like to acknowledge some of professors from my undergraduate studies that granted me research opportunities and valuable advise: Jon McGowan (UMass, Amherst), Steven Low (Caltech), Jesús del Álamo (MIT), Ram Rajagopal (Stanford), Gerson Beauchamp Báez (UPRM), Agustín Irizzary Rivera (UPRM), Eduardo Ortiz Rivera (UPRM).

Navigating the PhD was also significantly aided by important people in the Electrical Engineering and Computer Sciences Department and College of Engineering at UC Berkeley. In particular, I want to recognize the significant help I received from Audrey Sillers and Meltem Erol. They both helped out with many funding and logistical situations throughout my time at Cal and I truly appreciate their support, it was invaluable to my success. I also

want to to acknowledge Shirley Salanio and Jessica Gamble for also playing a significant role in my success. Lastly, I also want to acknowledge Judy Smithson's support as well.

I am lucky to have friends outside of my academic community who I would also like to acknowledge because it made my time during my PhD so much more joyful: Nick Van Eyck, Serena Wong, Whitney Nore. I also want to to thank my Cuban family Yanek Revilla, Yisel Cuba, and Silvia Bonne. And, of course, my Puerto Rican friends and in particular Héctor de Jesús Cortés.

Lastly, but of course not least, to my family Arnaldo, Jossie, Kamila for their unwavering support in me pursuing my goals and their desire to see me succeed.

Chapter 1

Introduction

The United States of America's (USA's) Cybersecurity and Infrastructure Security Agency identifies the so-called *energy sector* as "a multifaceted web of electricity, oil, and natural gas resources and assets to maintain steady energy supplies and ensure the overall health and wellness of the nation". They further assert its importance as a critical infrastructure sector providing an "enabling function" across all other critical infrastructure sectors such as agriculture, transportation, and healthcare therefore insisting on its pivotal societal role.

The backbone of the energy sector is the electric power grid. The power grid is the result of the interconnection of components and devices across its three primary subsystems: electricity generation, electricity transmission, and electricity consumption or loads. Example components include generating equipment to convert an energy source in its raw form into electricity, transmission line infrastructure to transport that electricity to where it is consumed, and end use devices by electricity consumers. This machine, the power grid, is therefore composed of many thousands of components spanning thousands of kilometers and therefore has extremely complex behavior; it is the largest machine ever built by humankind.

Consequently, not only is operating the grid reliably a critically important task due to its unparalleled societal role, but it is also an extremely complex machine on which to do so making this a significant engineering challenge.

In addition to an already difficult task, the grid has experienced dramatic changes in the last 25+ years due to three primary drivers: climate change, decreasing costs of renewable energy technologies, and development of technology. The first two drivers have meant that the raw energy source used for electricity generation has changed from fossil fuels such as oil, natural gas, and coal, to largely sunlight and wind. This means that the generating portfolio has changed from a inherently slow chemical, thermal, mechanical, and electrical process due to fossil fuels to a fast and mostly electrical one due to renewable energy sources, making the way the grid behaves and reacts inherently different. The third and last driver has meant that the kinds of devices that we are powering at the electricity consumption level are inherently different. Modern loads include large data centers, vehicles, and many consumer and household electronics due to major electrification trends to achieve better energy efficiency.

These trends are not expected to slow down any time soon and thus these drivers have induced changes on the grid at both the generation and consumption level. This implies that there are many new kinds of devices connecting on the power grid and play a role in how the grid behaves, yet their impact has not been studied in detail.

In this thesis, I present solutions to some of the new engineering challenges the modern power grid is facing due to the large and inherent changes occurring with the goal to ensure that we can reliably operate the most important critical infrastructure to society.

1.1 Drivers of change in the power grid

Climate change

Planet Earth's climate has been significantly changing since the start of the industrial revolution in the latter half of the 18th century, and it is the core driver for the large and continuous amounts of renewable energy technologies incorporated in modern power systems.

Power systems have historically been powered by burning fossil fuels such as natural gas, oil, and coal. When these chemical energy sources are burned to be converted to electricity they emit harmful greenhouse gases to the environment inducing a greenhouse effect on Earth's atmosphere. This effect traps sunlight inside the atmosphere and leads to rising temperatures affecting global climate. Figure 1.1 shows average global temperatures rising since 1880, with 2023 being the hottest year to record with a 1.2 °C increase relative to the 20th century average temperature. These rising temperatures have resulted in more frequent atmospheric events in recent decades including hurricanes, floods, and rising sea levels, which have consequently affected humans' quality of life.

Renewable energy sources such as solar photovoltaic panels, and wind turbines are able to convert energy from their original source into electricity without emitting greenhouse gas emissions as a byproduct.

Decreasing costs of renewable energy technologies

While climate change is a strong social incentive for a transition to renewable energy technologies, capitalistic decisions are driven by financial decisions. For many years it was the case that new power generation plants were of fossil fuel sources largely because they were cheaper. However, as of 2015, the levelized cost of energy [1] for solar and wind projects have dropped below that of all fossil fuel based sources. This implies that there is now a strong financial incentive for new energy generation projects to be of renewable energy nature. Figure 1.2 shows that as of 2011 onshore wind energy has a lower LCOE than most large fossil fuels, and utility-scale solar PV followed the same trend in 2015.

[1] Levelized cost of energy, or LCOE, is an estimate of how much it costs to generate each unit of energy from a power generation project over its lifetime.

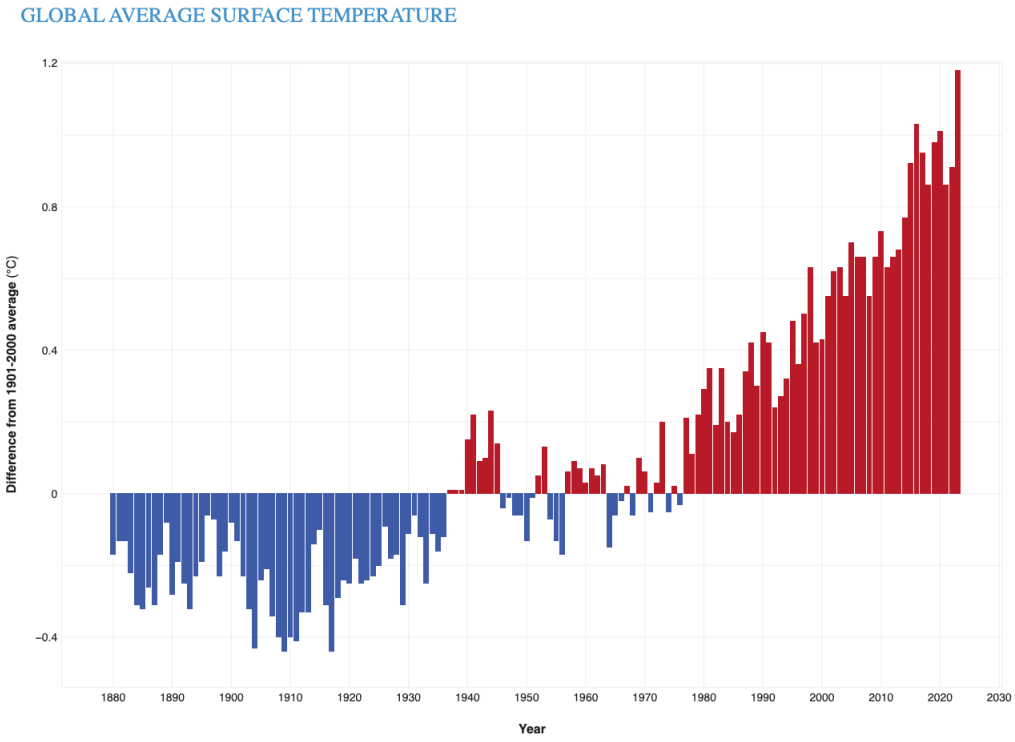

Figure 1.1: Average global surface temperature relative to 20th century average [16].

Due to these first two drivers, renewable energy projects at the generation level have therefore been seeing a rapid incorporation into modern power systems even resulting in large interconnection queues.

Development of new technologies

The 21st century has also seen much innovation in technology. Electric vehicles (EVs), for example, are no longer a rare sighting and have become ubiquitous in California (where this thesis is being written), and other major metropolitan areas as well. From the grid's perspective, this is a new kind of load that the grid needs to power because EV batteries are charged with direct rather than alternating current electricity. Furthermore, trends in electrification due to higher energy efficiency of electronic appliances have meant that domestic items such as stoves, water heaters, HVAC systems, will shift to being electrically powered, which are also direct current loads in nature.

This trend suggests a large shift in the kinds of devices that electricity consumers use that also means that the way they consume electricity is different than what has been the case for decades.

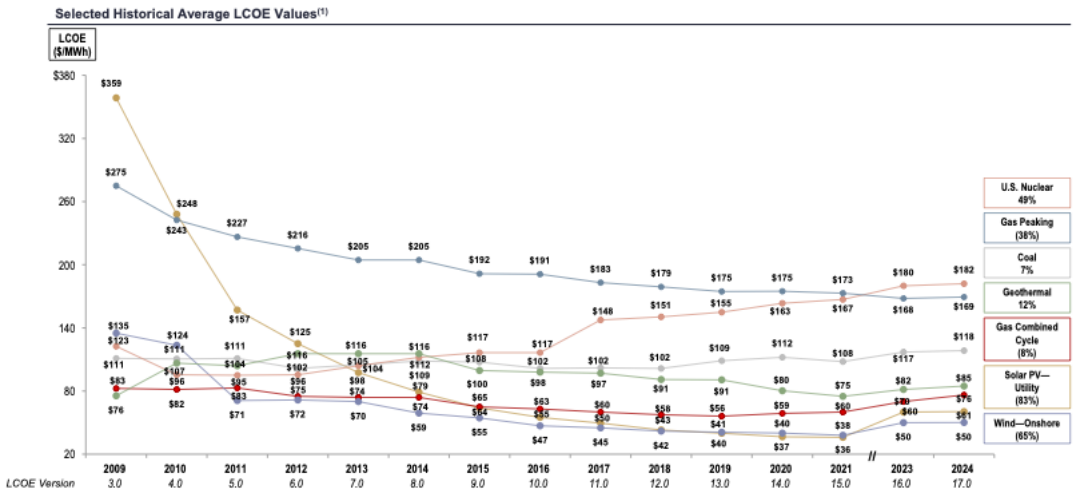

Figure 1.2: Average global surface temperature relative to 20th century average [6].

1.2 Changes in modern power systems

From a physics perspective, each device connected on the power grid, whether it is a generator, a transmission line, or load, has its own physical properties. This is based on the materials with which it is constructed that determine the way it consumes power, and the way each of them interacts with all other power grid components. In practice, the new kinds of device connected on the grid use new materials and in new configurations which changes the way electricity is generated and consumed. When this happens at a large enough scale, it can affect the aggregate level behavior of the network, which is what this thesis seeks to address.

Basic grid operation

Historically, the power grid has generated electricity by burning a chemical energy source and producing heat to boil water. When water turns to high-pressure steam it is able to spin a turbine, which in turn spins the rotor of a generator, and finally resulting in electricity through electromagnetic induction. Facilities where this process takes place are typically called thermoelectric plants. This process inherently involves many energy conversion steps: chemical $\rightarrow$ thermal $\rightarrow$ mechanical $\rightarrow$ electrical. Each of these energy conversion stages introduces physical behavior on the power grid which largely determines how the power grid behaves and reacts. By and large, this is the most popular way to generate electricity. Other energy conversion methods, while they may be slightly different, have the same result.

Perhaps the most important component in this energy conversion process is the generator, which we will call a synchronous generator (SG). Because of the physical construction of a SG, it inherently produces three voltage signals, or phases, of the same amplitude, same

frequency, and offset from each other by $\frac{2\pi}{3}$ radians. The voltage signal frequency is proportional to the frequency at which the rotor spins. Typically, this frequency is desired to be constant during nominal operation of the grid, and said frequency is referred to as the synchronous frequency, hence the name synchronous generator. Because the voltage waveforms produced by this physical process have a constant frequency, and thus change over time, this is referred to as alternating current (AC) electricity, contrary to direct current (DC) electricity which has a frequency of zero and is constant over time. This has meant that the grid has always been operated using AC electricity.

Further, because this energy conversion process has multiple stages, it takes a non-negligible amount of time to burn fuel to heat a large amount of water, to spin a turbine, and then a shaft to finally produce electricity. We will refer to this energy conversion process as a slow one from here forward.

New devices on the grid

On the generation side, renewable energy sources such as energy in the form of light produce electricity in a drastically different way relative to fossil fuels, and therefore behave differently. While thermoelectric plants have many energy conversion stages and are inherently slow, solar photovoltaic panels are able to instantaneously convert light into electricity by use of semiconductor materials. In this case there is only one energy conversion stage and it occurs much faster. Further, it inherently produces DC electricity, rather than AC electricity, so it needs to be converted to AC form to be compatible with the AC grid.

Wind turbines leverage aeolic energy in the wind to spin a shaft, in turn spinning a generator thus producing electricity. While this process has some similar stages to a thermoelectric plant, namely the turbine to generator connection, generators in thermoelectric plants are able to generate voltages at a constant frequency. Wind turbines, however, produce non-constant frequency AC electricity because they are at the behest of the wind blowing at any instant. This then needs to be converted to DC electricity, and then converted into a grid-compatible constant AC frequency signal.

Energy storage facilities, such as batteries, typically are DC sources which also need to be converted to grid compatible AC signals. Moreover, on the load side, electric vehicles, and most new electronic loads are DC loads. In order to connect to the grid, they need to take the AC grid electricity and convert it to DC to be usable.

The commonality among all these new technologies both on the generation and load side is that they interface with the existing grid through electronic circuits called power converters. Power converters are energy conversion devices which take energy in one form and convert it to another electrical form; they serve as the interface between AC and DC devices. In particular, inverters are a type of power converter that take DC electricity and convert it to AC electricity. Rectifiers, on the other hand, are power converters that operate in the opposite way by taking AC electricity and converting it to DC electricity. Oftentimes the same power converter can operate as both an inverter and a rectifier depending on which

direction power is flowing. That is, when power flow is one direction it operates as a rectifier, and when power flow is in the opposite direction, it operates as an inverter.

1.3 Motivation to study power systems with high fidelity models

These drivers of change for the power grid have meant that we are seeing more and more power converters on the grid. While power converters themselves are not new technology, the fact that so many of them are suddenly being connected on the grid means that they may have system level impacts, and understanding these is important for the reliable operation of the power grid.

One of the many differences between synchronous generators and power converters is that they operate on very different time scales. Converters are electrical devices with reaction times in the milli- and even microseconds. Generators, while they may have some fast dynamics as converters, are mainly driven by much slower dynamics due to the multi-stage energy conversion processes thus operating in multi-second and longer time scales.

Contrary to synchronous generators whose behavior is mostly determined by its physics, converters are highly controllable devices. They can be programmed to follow a particular set of instructions, meaning that their mathematical modeling can be difficult. Consequently, there is a strong need to revisit power system engineering studies in detail considering the new behavior introduced by power converters.

Mathematical modeling introduction

In order to perform studies of any kind for power systems, a description of the behavior of the system is needed. This description is typically in the form of a mathematical model. This can be an algebraic relationship between variables as equality constraints; Ohm's law

$$I_R(t) = V_R(t)/R$$

is an example which states that the current I_R flowing through a resistor with resistance R is proportional to the voltage V_R across it. Another description form could be a differential equation relating two variables, such as the current flowing through a capacitor which is a function of the time derivative of the voltage

$$I_C(t) = C\frac{d}{dt}V_C(t).$$

Modeling power systems is a very difficult task generally speaking. Power systems are so large, so complex, and play such an important societal role that plans need to be made about them anywhere from instantaneous decision making reacting to contingencies to 50-year-ahead planning. Therefore, the kinds of models used for the different kinds of analyses

depending on the time scale considered are radically different from each other and many simplifying assumptions need to be made to make problems tractable.

For example, one kind of study is a power flow study. In this case, the objective of the problem is to find an equilibrium point at which the system can operate stably: it is a steady state problem. Therefore all variable relationships are algebraic. The implicit assumption here is that the underlying generators have the controls in place to drive the system to this operating condition.

Another kind of study is a transient study. In this scenario, the power system undergoes a fault (e.g., a transmission line disconnecting), and reacts. One objective here can be to see how the system responds and to see if it can recover after the fault. In this case, more detailed differential equation models are needed for the different devices on the grid to describe the time evolution of the variables.

Beyond the models themselves, there are large amounts of uncertainty on the grid which make the choice of model very hard. For example, modeling load is an intrinsically difficult, or even impossible, task because it relies on predicting how humans will consume electricity. While there are good prediction algorithms based on weather patterns and consumer behavior, any model that tries to capture this behavior is an approximation that makes the problem tractable. Renewables only exacerbate the modeling task because of the inherent intermittency in the raw energy sources: sunlight is only available during the daytime and is easily reduced by clouds, and wind speeds can vary significantly throughout the course of a day. Therefore, often simplifications are made to be able to make the problem analyzable.

Moreover, modeling converters is also a difficult task because they typically have many subsystems, and also present hybrid dynamics: continuous-valued state dynamics in physical variables such as voltage and current, and discrete-valued state dynamics such as a switch being closed or open. Further, converters have much lower power ratings relative to generators, so while for a given application you might need one generator, you could need on the order of tens of converters to meet the same objective. This means that the modeling is even more complex because the system requires many more devices to meet the same objective.

Power systems are typically modeled as differential algebraic equations (DAEs) of the following form.

$$\begin{bmatrix} \dot{x} \\ 0 \end{bmatrix} = \begin{bmatrix} f(x, y, u) \\ g(x, y, u) \end{bmatrix} \tag{1.1}$$

Here, $x \in \mathbb{R}^n$ are the system's dynamic states, $y \in \mathbb{R}^m$ are the system's algebraic states, $u \in \mathbb{R}^p$ are the system inputs. $f : \mathbb{R}^n \times \mathbb{R}^m \times \mathbb{R}^p \to \mathbb{R}^n$ and $g : \mathbb{R}^n \times \mathbb{R}^m \times \mathbb{R}^p \to \mathbb{R}^m$ are the vector equations associated to the dynamics of the network and the algebraic constraints.

Depending on the type of study to be performed, a particular device, say a transmission line, can be modeled with an algebraic model, or a differential equation model. The choice will depend on the study's objective. This means that the states that describe the behavior of that device can show up in x or y in 1.1, depending on said choice. Further, the same device can be modeled with different number of equations depending on what kind of modeling

fidelity is desired. Therefore, the size of the state vectors x, y can change depending on the choice of model for devices. This allows for capturing simplified or more nuanced dynamics.

Lastly, it is important to have models that make sense relative to each other. That is, we must understand how some models will interact with others so that the results from a particular study make sense to analyze. Here a tradeoff between modeling complexity and analyzability is needed. That is, the higher the fidelity a model is desired, the more difficult it will be to solve that problem computationally. However, if not enough fidelity is included then there is a risk that the results will not hold the meaning that is desired because its assumptions may be flawed.

Modeling to replicate versus modeling to gain insight

An important distinction to be made is noting a difference between modeling with the objective to replicate or predict an event that occurred or could occur in a real power system versus modeling with the objective to gain insight about a power system's behavior.

The sheer size of power systems, their many layers, complexity, intermittency, make them next to impossible to model with absolute precision; in fact, more often than not, substantial simplifying assumptions need to be made in the modeling process in order to make the problem solvable. While scientific analyses are followed so that these approximations are justified, it is always a possibility that important information is unintentionally missed.

So in this thesis, one of the main motivations is to model power systems with the objective to gain insight on power systems' behavior at a system level, while relying on some scientifically rigorous assumptions.

1.4 Thesis contributions and organization

To this end, this thesis has several contributions aimed at understanding power system behavior in face of all the new challenges. Overall, it presents a holistic power system analysis from generation, to transmission, to load modeling, with both simulation-based empirical and theoretical contributions.

- Chapter 2 presents the first provably globally asymptotically stable control law for sinusoidal reference tracking for inverters considering switching and a grid forming control law in the form of droop control. This chapter includes contributions from Kaylene Stocking, Duncan Callaway, and Claire Tomlin.

- Chapter 3 presents a detailed analysis of the effect of transmission line models of varying fidelity on power systems' small signal and transient stability. It also presents a new open source simulation package for high-fidelity transmission line modeling `TLModels.jl` in the `Julia` programming language. This chapter includes contributions from Ruth Kravis, Sunash Sharma, Claire Tomlin, and Duncan Callaway.

- Chapter 4 presents the ZIP-E load, new kind of load model which captures the behavior of power electronic loads, along with detailed analysis of the effects of load models on system stability. It also presents a new open source simulation package for ZIP-E load modeling, `ZIPE_loads.jl`, in the `Julia` programming language. This chapter features contributions from Reid Dye, Claire Tomlin, and Duncan Callaway.
- Chapter 5 presents a detailed theoretical analysis of the relationship between *abc* and *dq* reference frame signals. It provides a one-to-one relationship between a signal in *abc* and how it decomposes into signals in *dq* and vice-versa.
- Chapter 6 concludes this thesis.

Chapter 2

Analysis, stability, and control of the half-bridge inverter using a hybrid model

As Chapter 1 has discussed, modern power grids are seeing a large portion of their generation replaced by renewable energy. Therefore, the energy conversion process is changing and converter-interfaced generation (CIG) systems, primarily in the form of power electronic inverters, are becoming the primary interface between energy sources and loads. In this chapter, we look to address some of these challenges at the generation level.

This chapter is based on the paper "Analysis, stability, and control of the half-bridge inverter using a hybrid model" presented at the 2023 European Control Conference in Bucharest, Romania. It was coauthored with Kaylene Stocking, Duncan Callaway, and Claire Tomlin.

2.1 Introduction

The Need for New Inverter Controls

Inverters are highly controllable devices that convert a DC energy source, like a solar photovoltaic panel, to a grid-compatible AC energy form. Since the number of inverters in the power grid is increasing, and because they react to programmable instructions, the design of control strategies for power grids with large numbers of CIGs is considered a problem of paramount importance in the low-inertia grid research community [45]. Emphasizing this point, in 2016 the European Union funded the MIGRATE (**M**assive **I**nte**grat**ion of Power **E**lectronic Devices) project [64] to study fundamental challenges associated with incorporating renewables in the grid. The team was composed of experts from over 20 participating institutions from industry and academia. Furthermore, in 2021, the United States of America's Department of Energy funded the UNIFI (**Uni**versal Interoperability for Grid-**F**orming

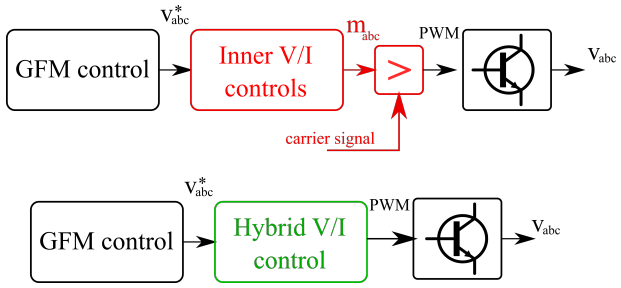

Figure 2.1: Above, the typical current and voltage inner controls for an averaged model inverter. Below, the proposed hybrid controller.

Inverters) Consortium [18], consisting of experts from over 40 participating institutions, to answer questions of a similar nature.

Recent work further recognizes the need to consider new control methodologies for inverters [53]. Accentuating this need, the IEEE task force for stability definitions and classification for low-inertia grids has specifically recognized the importance of hybrid systems analysis for the study of power and power electronic systems [23]. Hence, due to the importance that inverter control strategies will play in the future grid, we believe it is imperative to explore the whole landscape of possible controllers, including those that, as in this work, rely on the more physically realistic hybrid systems model of the inverter.

One approach to inverter control is the grid-forming (GFM) paradigm, in which the inverter is configured as a controllable voltage source with provisions that enable power sharing, among other system-level desired performance requirements. A future grid will likely need a large portion of its generation controlled via GFM controls [45].

Several GFM control strategies with strong theoretical guarantees have been proposed and validated through simulation and hardware experimentation [31, 3, 2, 50]. Their implementations thus far usually use a sinusoidal pulsed-width modulation (PWM) strategy whose analysis relies on the inverter averaged model and leads to the well-studied nested voltage and current feedback loop structure, shown above in Fig. 2.1, as the inner loop inverter controls [50]. In this context, a GFM control strategy instructs the inverter to achieve certain set points that have been optimized at a system level. The inner voltage and current control loops, in red, aim to drive the actual inverter variables to these references by translating them into a modulation signal for a pulse-width modulator. In this work, we propose replacing the inner loops with our hybrid control strategy, in green. Specifically, Fig. 2.1 presents the standard control architecture for an inverter (above), and our proposed hybrid control strategy (below) and how we envision it as an alternative.

By providing a fixed template for which new control strategies need to be compatible with, the averaged model and inner control loops constrain how new inverter controls can be implemented. Moreover, in simulation, they ignore the fast switching dynamics, which are on similar time scales as line voltage and current dynamics [23], thus potentially hiding some

dynamic interactions. Furthermore, some initial results point to the inner control loops as the primary culprits for instability in system-wide studies [50].

Therefore, in this chapter we propose a hybrid systems approach for the modeling, analysis, and design of a controller with a new structure meant to replace the inner voltage and current loops to address these concerns. As we will show in Section 2.3, the controller we present is not dependent on control gains that need to be tuned. This provides a promising path to ensure system stability and performance guarantees for system-wide studies, where studies that use the averaged model and inner PI control loops are dependent on the choice of controller gains. We believe this could provide a way to obtain trustworthy and generalizable system-level results. Specifically, Fig. 2.1 presents the standard control architecture for an inverter (above), and our proposed hybrid control strategy (below) and how we envision it as an alternative.

Hybrid Systems for Power

Even though power and power electronic systems inherently exhibit hybrid dynamics, the field of hybrid systems has only seen limited use in the context of its stability analysis and control design.

Most of the known work in this space has attempted to model general power system problems within a hybrid dynamical systems framework. For example, some applications include the modeling of continuous-valued state variables (e.g., currents and voltages) in systems with discrete-valued control or protection actions (e.g., circuit breaker operation) [28]. Other work has modeled the variation of system-level inertia in the swing equation in a hybrid dynamical systems framework [26].

In the power electronics literature, hybrid systems theory has been primarily used in the context of DC-DC converters. One of the first reported uses of a hybrid systems framework for power electronic converters was in [61], where the authors derive conditions for a safe set and design a hybrid control law to maintain the system state within this set. Further work derives a set of control laws, also for DC-DC converters, that achieve global, asymptotic stability to the desired operating point [8].

More recently, some of these ideas have started to appear in the control of power electronic inverters, for which the desired reference signal is a time-varying sinusoid instead of a constant setpoint [1]. The authors of [1] derive a model for the half-bridge inverter in error coordinates and show that the solution of an optimization problem leads to the desired behavior. More work in this space has also been pursued through sliding mode control ideas for inverters connected to an infinite bus [36, 35].

Summary of Contributions

Specifically, beyond prior results in [1], this chapter's contributions include i.) an explicit, closed-form expression for a globally-asymptotically stabilizing hybrid control law for the half-bridge inverter that needs no tuning, ii.) an analytical derivation for a global Lyapunov

function that proves uniform, global, asymptotic stability of the origin in error coordinates thus achieving the tracking of the reference signal for a hybrid inverter model, iii.) a method to update the controller to be robust against resistive load changes, iv.) analysis and validation of the controller in simulation, and v.) a demonstration in simulation of the controller's operation in conjunction with a grid-forming control strategy, suggesting the potential of hybrid systems-based control in this practical context.

We further aim to aid understanding of the control scheme by interpreting the controller's behavior, including finding an underlying switching surface. We note that, while the designed controller itself is a switching policy, we call it a hybrid control law because it is implemented in a hybrid dynamical system environment.

Chapter Organization

The rest of the chapter is organized as follows. Section 2.2 presents the notation and problem formulation, Section 2.3 presents our theoretical results, and Section 2.4 our experimental results. Finally, Section 2.5 concludes the chapter and discusses limitations and future work.

2.2 Problem Formulation

In this section, we present our modeling approach for the half-bridge inverter and the control problem we aim to solve. The model we use was first proposed in [1].

Notation

Dot notation indicates the time derivative of a variable, i.e., $\dot{x} = \frac{dx}{dt}$. Bold-faced capital letters will indicate matrices. $\sigma(\mathbf{A})$ is the spectrum of $\mathbf{A}$, and $\lambda_{\mathbf{A}}$ an eigenvalue of $\mathbf{A}$. $\|\cdot\|$ is the Euclidean vector norm. The operator $sign(\cdot)$ returns $+1$ if its scalar argument is greater than or equal to zero, and -1 otherwise. The operator $Re\{\cdot\}$ takes the real part of its argument.

Switched Model

We study the half-bridge inverter shown in Fig. 2.2. It is composed of a midpoint-grounded voltage source V_{DC}, a pair of switches, and an LC filter. It delivers power to an arbitrary load. We consider a resistive load, R, as the natural first case study. Future work may consider RLC loads, ZIP loads (constant impedance, Z, current, I, and power, P), and grid interconnections.

We define two discrete states: i.) SW1 on and SW2 off, and ii.) SW1 off and SW2 on. We also define the control input to be $u \in \{+1, -1\}$, where $u = +1$ denotes the first discrete operating state, and $u = -1$ denotes the second. We define the state vector as $x = \begin{bmatrix} v_C & i_L \end{bmatrix}^\top \in \mathbb{R}^2$, where v_C and i_L are the capacitor voltage and inductor current, respectively.

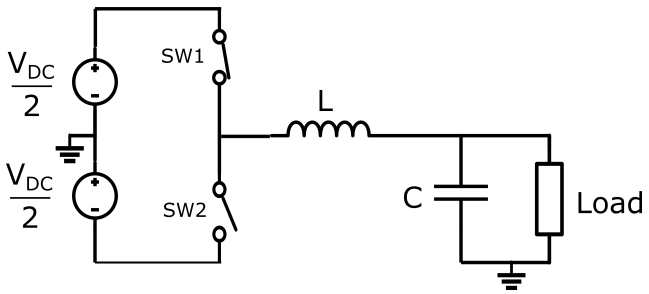

Figure 2.2: The half-bridge inverter.

Applying Kirchhoff's current and voltage laws to model the voltage and current dynamics for each discrete state, we obtain equation (2.1a). Conveniently, the choice of control input, $u \in \{+1, -1\}$, characterizes the inverter's terminal voltage polarity in Kirchhoff's voltage law equations such that the dynamic evolution of both discrete states can be compactly characterized by a single equation, (2.1a). The model describes a linear, time-invariant (LTI) dynamical system with a binary-valued, discrete control input.

$$\dot{x} = \mathbf{A}x + \mathbf{B}u \tag{2.1a}$$

$$\mathbf{A} = \begin{bmatrix} -\frac{1}{RC} & \frac{1}{C} \\ -\frac{1}{L} & 0 \end{bmatrix}, \ \mathbf{B} = \begin{bmatrix} 0 \\ \frac{V_{DC}}{2L} \end{bmatrix} \tag{2.1b}$$

Designing the Reference

The control objective is for v_C to track a sinusoidal reference signal. Following [1], we first define an oscillator system that produces the appropriate reference signal. Then, we reformulate the dynamical system in terms of error from the desired reference state.

We denote the reference vector $x_{ref} = \begin{bmatrix} v_{C,ref} & i_{L,ref} \end{bmatrix}^\top$. We choose a sinusoidal voltage reference $v_{C,ref}(t) = V_m \sin(\omega t)$, with amplitude V_m and frequency ω, both being design parameters. Kirchhoff's laws allow us to express the appropriate inductor current reference $i_{L,ref}$ in terms of these parameters as $i_{L,ref}(t) = \omega C V_m \cos(\omega t) + \frac{1}{R} V_m \sin(\omega t)$.

To design the reference, we define an oscillator system of the form of (2.2).

$$\dot{z} = \mathbf{\Theta} z = \begin{bmatrix} 0 & \omega \\ -\omega & 0 \end{bmatrix} z \tag{2.2}$$

Note that $\mathbf{\Theta}$ is a skew-symmetric matrix with eigenvalues $\lambda_{\mathbf{\Theta}} \in \{+j\omega, -j\omega\}$ defining an oscillator. Therefore, we know that, for a given initial condition, which can arbitralily be chosen as $z(t = 0s) = V_m \begin{bmatrix} 0 & 1 \end{bmatrix}$, $z(t) = \begin{bmatrix} V_m \sin(\omega t) & V_m \cos(\omega t) \end{bmatrix}^\top$.

We define our state reference to be a linear transformation of the oscillator state, z, to

achieve x_{ref} by

$$x_{ref} = \mathbf{\Pi} z = \begin{bmatrix} 1 & 0 \\ \frac{1}{R} & \omega C \end{bmatrix} z. \tag{2.3}$$

We further compute the reference dynamics to arrive at (2.4c).

$$\dot{x}_{ref} = \mathbf{\Pi}\dot{z} \tag{2.4a}$$
$$= \mathbf{\Pi}\mathbf{\Theta} z \tag{2.4b}$$
$$= (\mathbf{A}\mathbf{\Pi} + \mathbf{B}\mathbf{\Gamma})z, \tag{2.4c}$$

where

$$\mathbf{\Gamma} = \frac{2}{V_{DC}} \begin{bmatrix} \omega \frac{L}{R} & (1 - \omega^2 LC) \end{bmatrix} = \frac{2}{V_{DC}} \begin{bmatrix} \Gamma_1 & \Gamma_2 \end{bmatrix}. \tag{2.5}$$

Our subsequent analysis will be simplified by defining the state error from the reference signal as $e = x - x_{ref}$. Combining equations (2.1a) and (2.4c), we have that

$$\dot{e} = \mathbf{A}x + \mathbf{B}u - (\mathbf{A}\mathbf{\Pi}z + \mathbf{B}\Gamma z) \tag{2.6a}$$
$$= \mathbf{A}e + \mathbf{B}(u - \mathbf{\Gamma}z). \tag{2.6b}$$

Together, equations (2.2) and (2.6b) define the system dynamics.

Now that we have fully characterized the system dynamics in error coordinates, the problem we are trying to solve is to find a control law $u(t)$ that drives the error coordinates to the origin, implying that the system states will track the desired reference signals in the original coordinates.

2.3 Global Asymptotically-Stable Reference Tracking

In this section, we present our theoretical stability results including i.) the derivation of an explicit control law with a proof that this control drives the reference error to the zero state, ii.) an analytical solution to the Lyapunov equation as a function of the system's parameters, and iii.) a proof showing that we can appropriately adjust our control law to be robust against known changes in load, and still track the desired trajectory.

Global Asymptotic Stability Result

Theorem 1. *Consider the dynamical system* (2.6b). *Let* $\mathbf{A}$ *be Hurwitz, i.e.* $Re\{\lambda_{\mathbf{A}}\} < 0 \quad \forall \lambda_{\mathbf{A}} \in \sigma(\mathbf{A})$, *and let* $\|\mathbf{\Gamma}\| < \frac{1}{V_m}$. *Let* $\mathbf{P} \in \mathbb{R}^{2\times 2}$ *be the symmetric, positive-definite matrix that satisfies the Lyapunov equation,* $\mathbf{A}^\top\mathbf{P} + \mathbf{P}\mathbf{A} = \mathbf{Q}$, *for a negative definite* $\mathbf{Q}$. *The existence of such a* $\mathbf{P}$ *is guaranteed by the assumption that* $\mathbf{A}$ *is Hurwitz [9]. Then, the switching policy*

$$u = -sign(\mathbf{B}^\top\mathbf{P}e) \tag{2.7}$$

results in the uniform, global, asymptotic stability of the origin for the error dynamics (2.6b).

Proof. We propose the candidate Lyapunov function $V(e) = e^\top \mathbf{P} e$, which is globally positive definite [60]. Taking its time derivative, we have that

$$\dot{V}(e) = e^\top (\mathbf{A}^\top \mathbf{P} + \mathbf{P}\mathbf{A}) e + 2(u - \mathbf{\Gamma} z)\mathbf{B}^\top \mathbf{P} e. \tag{2.8}$$

Furthermore, using our knowledge of the oscillator state, $z(t)$, which we know is stable by construction, we have that

$$\mathbf{\Gamma} z = V_m \frac{2}{V_{DC}} (\Gamma_1 \sin(\omega t) + \Gamma_2 \cos(\omega t)), \tag{2.9a}$$

$$= V_m \left\| \mathbf{\Gamma} \right\| \sin(\omega t + \psi),\ \psi = \arctan(\Gamma_1 / \Gamma_2), \tag{2.9b}$$

$$\Rightarrow |\mathbf{\Gamma} z| \leq V_m \left\| \mathbf{\Gamma} \right\|,\ \ \forall t. \tag{2.9c}$$

Therefore, the worst case magnitude for $u - \Gamma z$, i.e., $\max._z \{u - \mathbf{\Gamma} z\}$, is obtained when $\sin(\omega t + \psi) = -1$. So, we can upper bound $\dot{V}(e)$ using the Lyapunov equation and (2.9c) to yield the following.

$$\dot{V}(e) \leq e^\top \mathbf{Q} e + 2(u + V_m \left\| \mathbf{\Gamma} \right\|_2) \mathbf{B}^\top \mathbf{P} e \tag{2.10}$$

We know the term $e^\top \mathbf{Q} e \leq 0,\ \forall e$. Therefore, to ensure stability, we force the second term, $2(u + V_m \left\| \mathbf{\Gamma} \right\|_2) \mathbf{B}^\top \mathbf{P} e$, to also be less than or equal to zero using the following. Since by assumption $\left\| \mathbf{\Gamma} \right\|_2 < \frac{1}{V_m}$, and $u \in \{+1, -1\}$ by design, then the term $u + V_m \left\| \mathbf{\Gamma} \right\|_2$ will take the sign of u. By choosing a switching policy defined as $u = -sign(\mathbf{B}^\top \mathbf{P} e)$ under the stated assumptions, the second term will always be less than or equal to zero, and $\dot{V}(e) \leq 0$ always holds, implying that $V(e)$ is a valid, global Lyapunov function for the given dynamics. We can thus conclude that the origin in error coordinates is a uniformly-, globally-, asymptotically-stable equilibrium point. The states will track the desired trajectories in the original coordinates. □

It is worth noting that the assumptions required for this theorem are not very restrictive. For a passive RLC circuit as we have here, it can be proven that the eigenvalues of $\mathbf{A}$ will always have strictly negative real parts. Moreover, $\left\| \mathbf{\Gamma} \right\|_2 < \frac{1}{V_m}$ is easily satisfied for a wide range of realistic parameter values.

It is also worth noting that the control policy (2.7) is conservative since (2.10) is a worst-case upper bound for the Lyapunov function: it is only reached when $\sin(\omega t + \psi) = -1$. This implies that it is, potentially, inherently robust to some disturbances. In fact, it can be shown that this kind of formulation is actually robust with respect to disturbances [34].

Intepretation of The Control Result

Main theorem condition

The main theorem condition is $\left\| \Gamma \right\|_2 < 1/V_m$. It turns out that $\Gamma_2 = 1 - \omega^2 LC = 0$ because it is the filter design equation for its resonant frequency. This implies that the theorem

condition reduces to

$$V_m < \frac{1}{\omega}\frac{R}{L}\frac{V_{DC}}{2}. \tag{2.11}$$

This condition can be interpreted as a requirement on the amplitude of the desired sinusoidal voltage amplitude, V_m, to be strictly less than a scaling of the DC link voltage, V_{DC}.

In particular, a larger ω, smaller, R, and larger L make the bound tighter, implying it is harder to control because there is less slack on the bound. This is intuitively reasonable because high frequency implies a faster changing reference to track, a smaller R implies larger power consumption at the load, and a larger L implies current is more stiff to change, all of which intuitively make tracking the reference signal more difficult. A larger V_{DC}, meaning a larger buffer in the DC link voltage, will also lead to more slack on the bound.

Control action

The derived control law is a switching-based control, however, in this context it does not come with the traditional concerns for dynamic systems. For example, chattering, which is usually undesirable, is actually an inherent property of inverters: they are designed to execute extremely fast switching between discrete states to achieve the desired sinusoidal reference tracking, and the filter is designed to remove the higher order harmonics. Moreover u solely determines the discrete state of the system, and does not inject any signal directly by feedback, therefore there is no potential for high-gain injection either.

An underlying switching surface

The control law (2.7) can be interpreted as a switching decision based on whether or not the dynamics are over or under a specific hyperplane in a two dimensional state space. This is because of the use of the sign function: the control law is evaluating if the dynamics in the state space lie over or under the hyperplane defined by $\mathbf{B}^\top \mathbf{P} e = 0$. If it is over this hyperplane, then the $sign(\cdot)$ function will return a $+1$, and a -1 otherwise. This means that the hyperplane can further be interpreted as a switching surface, or a sliding mode.

Explicit Lyapunov Function in Terms of R, L, and C

In general, finding an explicit Lyapunov function that guarantees stability of a hybrid dynamical system can be difficult, even if each discrete dynamic state is LTI. To do this, researchers often resort to semidefinite optimization programs [7]. However, since the error coordinate dynamics (2.6b) reduce our system model to a single set of LTI dynamics, we can calculate the appropriate $\mathbf{P}$ matrix that satisfies the Lyapunov equation, $\mathbf{A}^\top \mathbf{P} + \mathbf{P}\mathbf{A} = \mathbf{Q}$, by solving a system of linear equations.

In this section, we show that this procedure allows us to express the $\mathbf{P}$ matrix explicitly in terms of arbitrary load and inverter parameters, R, L, and C.

Noting that $\mathbf{P}$ is symmetric, we have that

$$\mathbf{P} = \begin{bmatrix} p_{11} & p_{12} \\ p_{21} & p_{22} \end{bmatrix}, \tag{2.12}$$

where $p_{12} = p_{21}$.

Selecting $\mathbf{Q} = -\mathbf{I}$, the matrix equation $\mathbf{A}^\top \mathbf{P} + \mathbf{P}\mathbf{A} = -\mathbf{I}$ evaluates to

$$\begin{bmatrix} \frac{-2p_{11}}{RC} - \frac{2p_{12}}{L} & \frac{p_{11}}{C} - \frac{p_{12}}{RC} - \frac{p_{22}}{L} \\ \frac{p_{11}}{C} - \frac{p_{12}}{RC} - \frac{p_{22}}{L} & \frac{2p_{12}}{L} \end{bmatrix} = -\begin{bmatrix} 1 & 0 \\ 0 & 1 \end{bmatrix}. \tag{2.13}$$

We can use this equality to solve for p_{11}, p_{12}, and p_{22}. Doing so gives us an explicit solution for $\mathbf{P}$ in (2.14), as desired.

$$\mathbf{P} = \frac{1}{2}\begin{bmatrix} RC + \frac{RC^2}{L} & -C \\ -C & RL + \frac{L}{R} + RC \end{bmatrix} \tag{2.14}$$

Therefore, a function $V(e) = e^\top \mathbf{P} e$, with $\mathbf{P}$ given by (2.14), is guaranteed to be a global Lyapunov function for the dynamical system (2.6b) for the designed controller.

Remark. *While* $\mathbf{Q}$ *is oftentimes parameterized with some coefficient* $\alpha > 0$ *for tuning purposes in these kinds of proofs,* $\mathbf{Q} = -\alpha\mathbf{I}$ *for example, it can be proven that in this scenario, because of the use of the sign*$(\cdot)$ *operator, there is no change in the control decision when* α *is introduced. Therefore, this controller requires no tuning.*

What can be done, however, is to make a different choice of $\mathbf{Q}$*, which will change* $\mathbf{P}$*. This in turn will affect the slope of the switching surface defined by* $\mathbf{B}^\top \mathbf{P} e = 0$ *which can be chosen to prioritize* e_1 *or* e_2*.*

Controlling for Known Changes in Load

One motivation for finding an analytical expression for $\mathbf{P}$ is to handle changes in the system parameters. Note that our control policy, (2.7), relies on knowing $\mathbf{P}$. For example, if the load resistance, R, or filter parameters, L or C, change, the $\mathbf{A}$ matrix that defines the inverter dynamics in (2.1a) will change accordingly, and the switching strategy derived in section 2.3 may no longer achieve reference tracking if we do not update $\mathbf{P}$ to reflect that change.

We have shown that we can use (2.7) to asymptotically drive the states to our desired sinusoidal reference signals. Moreover, we have shown that for a specific choice of R, L, C parameters, we can analytically compute a $\mathbf{P}$ matrix which makes $V(e) = e^\top \mathbf{P} e$ a global Lyapunov function for the dynamical system, and thus we can implement our control law with such a $\mathbf{P}$.

Based on these two arguments, we now make the claim that if the system load changes, that is, R changes, and we know both loading scenarios, we can update our control law, (2.7), through (2.14) at the time the load changes. This, however, assumes that the load does not continuously switch between different R values too quickly, i.e. it's a step disturbance in the

Parameter	Symbol	Value
Load resistance	R	14.4 Ω
Inverter inductance	L	9.6 mH
Inverter capacitance	C	0.7 mF
DC supply voltage	V_{DC}	1,200 V
Target (reference) frequency	f	60 Hz
Target (reference) angular frequency	ω	$2\pi f \frac{\text{rad}}{s} \approx 377 \frac{\text{rad}}{s}$
Target (reference) magnitude	V_m	$120\sqrt{2}$ V ≈ 170 V

Table 2.1: Parameter values used for simulation experiments.

load. This will allow the control to still asymptotically drive the error state to the origin [44]. This is a reasonable assumption from the power and power electronics systems perspectives.

We provide validation through simulation for these three theoretical results in the following section.

2.4 Controller Validation Through Simulation

In this section, we test in simulation the performance of our switching controller.

The simulation parameters are shown in Table 2.1. L is designed to have a 30% inductor current ripple, a common practice in power electronics [58], while C completes the filter design to have a resonant frequency of 60 Hz with low gain. R is chosen as the nominal load equivalent to a power draw of 1 kW at the nominal operating voltage.

The inverter operates at a 10 kHz switching frequency, and we implement a simulation update frequency of 1 MHz. We also try a 100 kHz switching frequency for some experiments. These are realistic switching frequencies. We assume the switches are ideal: operating instantaneously and without losses.

Asymptotic Stability Under Constant Load

We first test the performance of our controller at recovering the target reference signal when starting from an off-reference initial condition. As shown in Fig. 2.3, we show accurate tracking of the desired reference signal. Subfigure a) shows the controller driving the inverter voltage, v_C, to the reference signal voltage, $v_{C,ref}$, when there is a 240 V difference in the initial condition at $t = 0$ s. The second panel shows the reference tracking error over time. Subfigure b) shows the trajectory of the system in the state space defined by the error coordinates. We see how the trajectory evolves over time in the state space and how the hyperplane defined by $\mathbf{B}^\top \mathbf{P} e = 0$ indeed is a switching surface and a sliding mode: our controller drives the reference tracking error towards the origin in error coordinates.

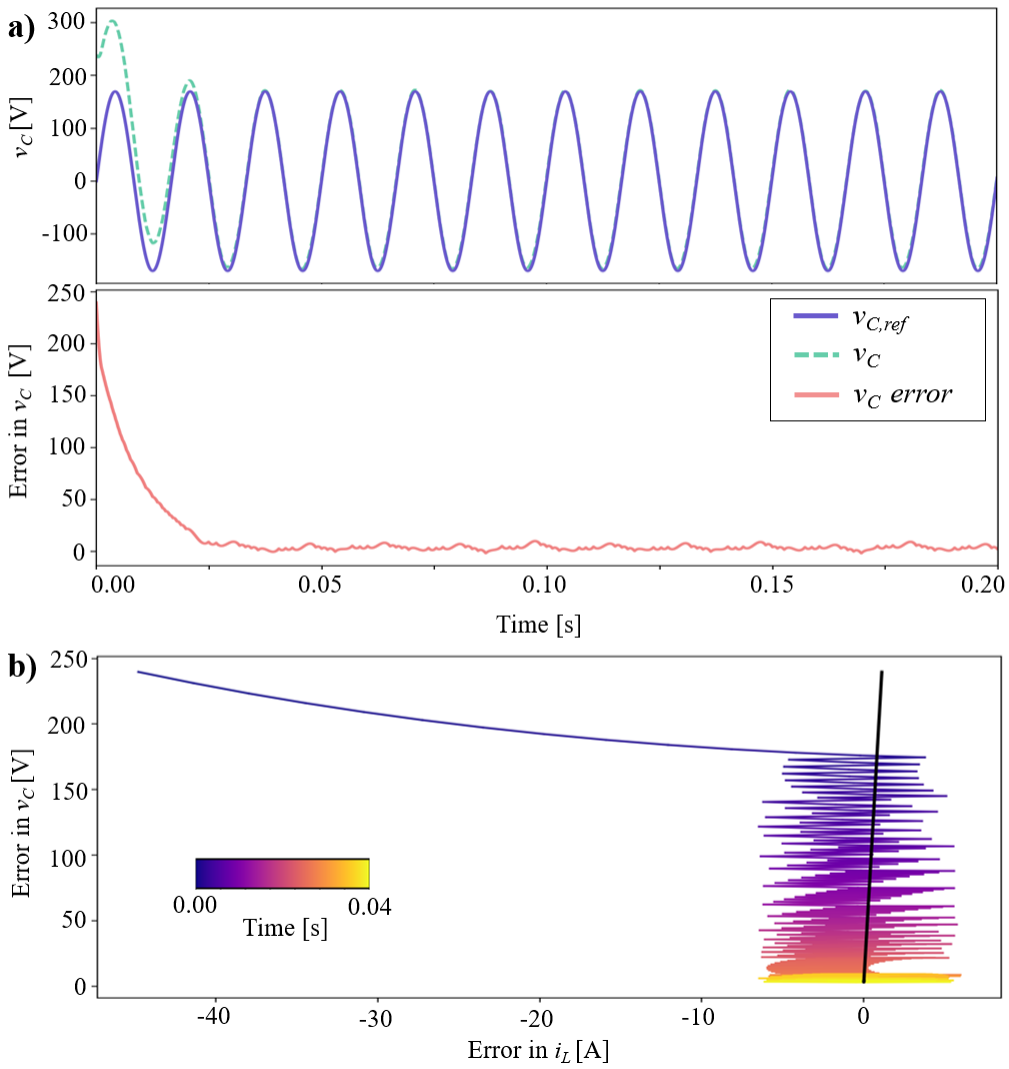

Figure 2.3: Time domain evolution of device dynamics in voltage coordinates, error coordinates, and state-space coordinates.

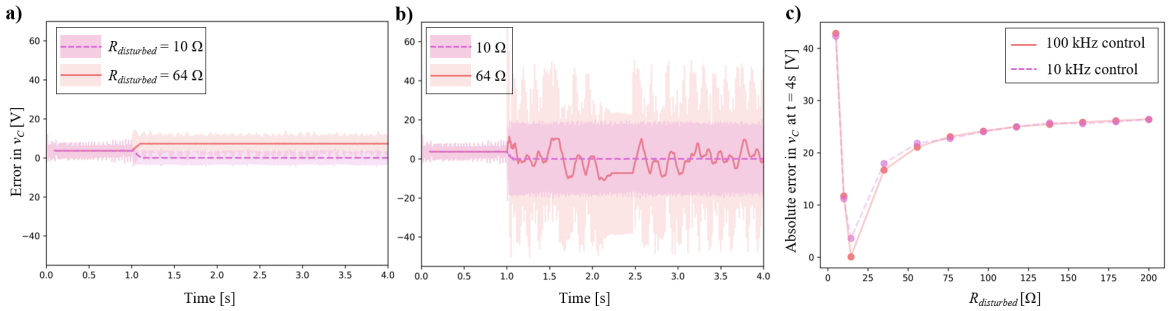

Figure 2.4: Controller performance under known and unknown changing load conditions. a) loading condition is changed to $R_{disturbed} = 10\ \Omega$ and $64.4\ \Omega$ at $t = 1.0$ s. b) The same load disturbances for a non-updated controller. c) Time-averaged absolute tracking error at $t = 4$ s for a variety of load conditions when the controller is not updated.

Stability Under Changes in Load

If the loading conditions change, we can ensure continued tracking of the reference by updating the control policy (2.7) through $\mathbf{P}$ in (2.14), as described in section 2.3. We validate this result in simulation by changing our initial load of $R = 14.4\ \Omega$ to different values during the simulation. We show our controller's performance under known and unknown changing load conditions in Fig. 2.4. In subfigure a), we change our loading condition to $R_{disturbed} = 10\ \Omega$ and $64.4\ \Omega$ at $t = 1.0$ s. Updating our 10 kHz controller in real time maintains accurate tracking of the reference signal, as evidenced by small error. That is, a controller updated through $\mathbf{P}$ with the new R continues tracking the reference after a switch to $R_{disturbed} = 10\ \Omega$ or $64.4\ \Omega$. In subfigure b), the we apply same load disturbances for a non-updated controller. $R_{disturbed} = 10\ \Omega$ has increased error but smooth averaged behavior. $R_{disturbed} = 64.4\ \Omega$ causes larger amounts of error. Lastly, in subfigure c), we plot the time-averaged absolute tracking error at $t = 4$ s for a variety of load conditions when the controller is not updated. These results suggest that the updated controller is robust to parameter changes, and even when updating is not possible the controller may still exhibit reasonable performance.

Updating the controller in response to load changes allows us to guarantee continued global, asymptotic stability. Moreover, empirically we find that for small disturbances an unmodified controller may also perform well. However, stability is lost for large disturbances such as a load change to $5\ \Omega$, as shown in panels b) and c) of Fig. 2.4.

Stability Under Extreme Reference Values

Since the result of Theorem 1 assumes that $\|\mathbf{\Gamma}\|_2 < \frac{1}{V_m}$, and $\|\mathbf{\Gamma}\|_2$ depends on ω, our controller is not guaranteed to track a reference signal for all possible combinations of V_m and ω.

In Fig. 2.5 we increase the amplitude, V_m (top), while keeping frequency fixed at $\omega =$

120π rad s^{-1} which we can see can prevent our controller from tracking the reference signal accurately. Analogously, increasing the angular frequency, ω (bottom) while keeping $V_m = 120\sqrt{2}$ V fixed results in the same behavior. This occurs because the assumptions of Theorem 1 no longer hold, which for our parameter values is good agreement with our theoretical results. The dotted vertical line shows the cutoff value for each parameter predicted by (2.11).

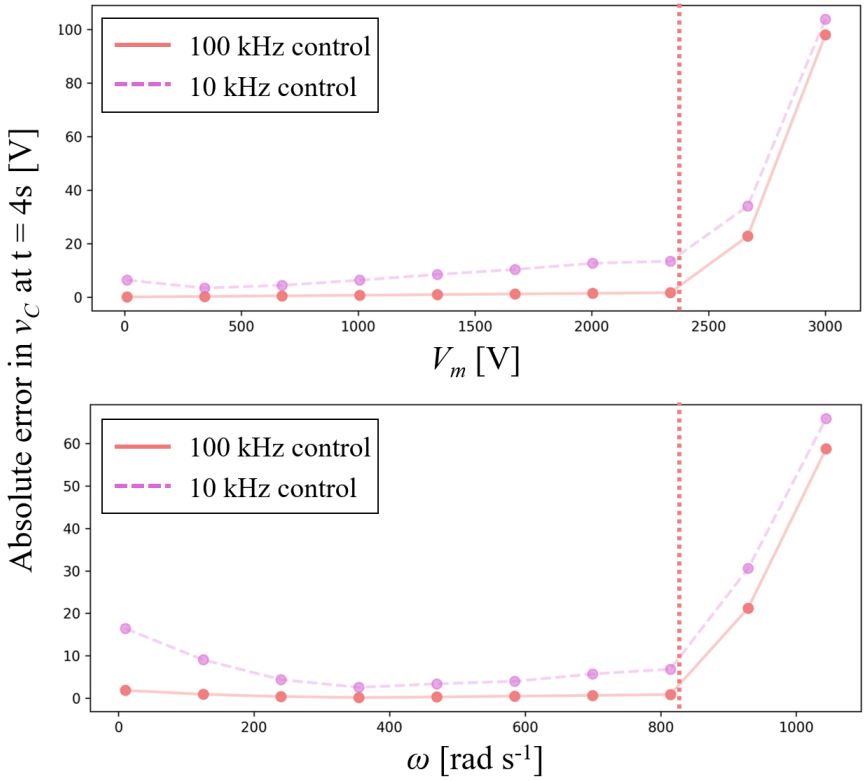

Figure 2.5: Increasing the amplitude, V_m (top), while keeping frequency fixed at $\omega = 120\pi$ rad s^{-1} and increasing the angular frequency, ω (bottom) while keeping $V_m = 120\sqrt{2}$ to test theoretical limit of the controller.

Layering a Grid-Forming Control Strategy

Until now, we have only focused on having the inverter track a sinusoid with a constant amplitude and frequency. In practice, inverters will regulate their sinusoidal voltage amplitude and frequency based on a predetermined GFM control strategy. In general, these try to optimize for some system-level operation criteria, for example, power sharing, frequency regulation, or a stability metric. Examples in the literature include droop control, virtual

oscillator control, synchronous machine emulation, and matching control, among others [31, 3, 2, 50].

These control strategies have been implemented in the past using the inverter averaged model, and the inner voltage and current loop structure [67]. However, in this work, we use simulations to explore the performance of our hybrid control strategy while layering on top a GFM control strategy. We choose droop control as an example.

Remark. *Droop control is often used in the context of power sharing and frequency regulation in a network of generators or inverters. In this experiment, we use droop control as an established way to change the voltage amplitude and frequency to determine the ability of our proposed controller to handle continuous changes in reference values, rather than to test synchronizing or power sharing capabilities.*

Droop control regulates the rms voltage, $V_{rms} = V_m/\sqrt{2}$, and frequency, ω, of the reference signal according to the following equations.

$$\omega = \omega^* + k_p(P^* - P) \tag{2.15a}$$

$$V_{rms} = V_{rms}^* + k_q(Q^* - Q) \tag{2.15b}$$

Here P^* and P represent, respectively, the setpoint and measured values for real power supplied by the inverter while Q^* and Q represent, respectively, setpoint and measured values for reactive power. $V_m^* = \sqrt{2}V_{rms}^*$ and ω^* are the setpoint values for the reference signal, and k_p and k_q are the droop coefficients [50].

For our experiment, we begin with $V_{rms}^* = 120$ V and $\omega^* = 120\pi$ $\frac{\text{rad}}{\text{s}}$, as before. We change the steady-state real power being drawn by the resistive load as given by

$$P = \frac{V_{rms}^2}{R} = 1.44 \text{ kW}$$

by changing the load to $R = 10\ \Omega$. Although Theorem 1 does not guarantee stability under *continuously* changing setpoints provided by droop control, we find that, for values of $k_p = 0.01$ $\frac{rad/s}{W}$ and $k_q = 0.0025$ $\frac{V}{VAR}$, our controller is able to track the changing reference very well, as shown in Fig. 2.6.

Benchmarking Against the Averaged Inverter Model and PI Control Loops

To study the performance of our controller, we compare it against the state-of-the-art control architecture: droop control as the GFM control strategy with the well-known inner PI control loops for the averaged inverter model. We implement the nested PI control architecture and averaged inverter model as in [50]. Our PI controller gain design is inspired by [15].

We perform the same droop simulation for both cases with the aforementioned droop parameters. Fig. 2.6 shows our results: the behavior of our hybrid controller and an averaged

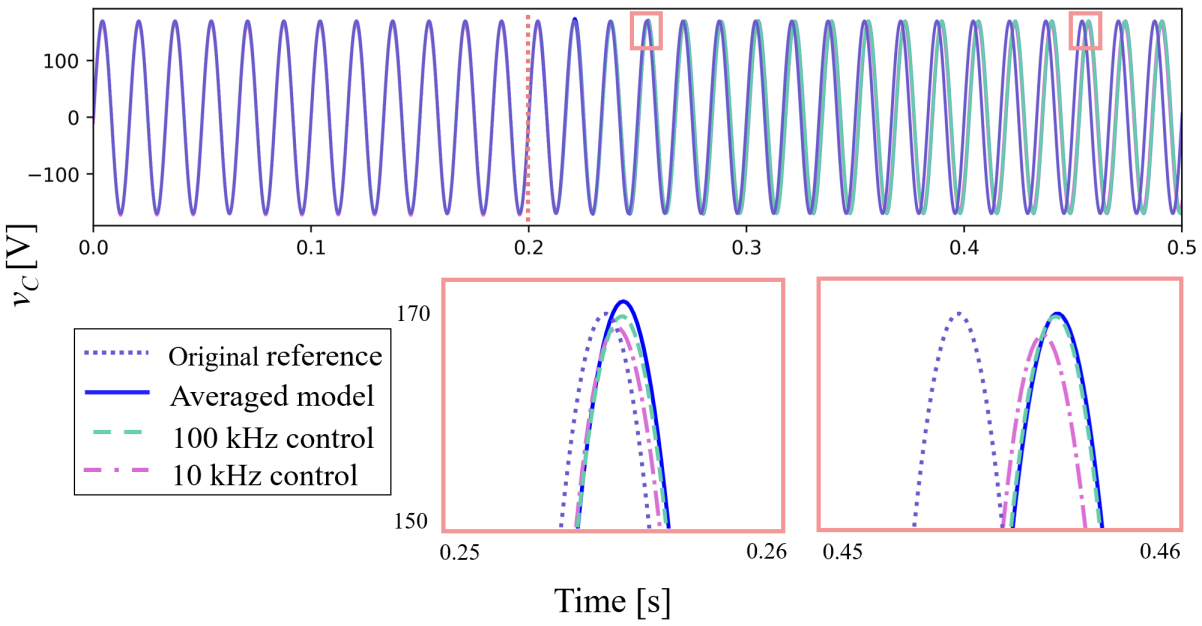

Figure 2.6: We show the behavior of our hybrid controller and an averaged model controller when the voltage amplitude and frequency set points are provided by GFM droop control.

model controller when the voltage amplitude and frequency set points are provided by grid-forming droop control. In this example, the real power being drawn by the load is changed at $t = 0.2$ s, when the load resistance drops from 14.4 Ω to 10 Ω, and droop control decreases the frequency of the reference as a result. The bottom panels show zoomed-in sections of the reference signal at the original frequency as well as the inverter v_C for the hybrid controller and averaged model controller. It can seen how before the disturbance at $t = 0.2$ s, both the PI control loops and our hybrid model perfectly track the desired sinusoidal reference signal. After the change in load, we can see how the both the voltages lag the 60 Hz reference because droop control instructs the actual voltage signals to slow down. We see how our hybrid approach matches the averaged model and PI controllers very closely.

Remark. *It is worth mentioning that the averaged model and PI controllers have some benefits in this simulation that would not be seen in practical application. Specifically, this approach does not account for any kind of switching. In practice, the averaging is used for a sinusoidal PWM strategy which determines the ON/OFF states of the transistors. This behavior is not captured in this simulation, thus showing idealized behavior in the simulation that will not be seen in practice, and making the comparison favor the averaged model and PI control approach. Future work will address this comparison in more detail.*

2.5 Discussion and Conclusions

As the power grid transitions away from fossil fuel-based generation, it is expected that increasing numbers of DC energy sources will supply power to the grid.The stability results we present are a step to tackle some of the challenges that arise in ensuring reliability of the grid with increased numbers of CIGs.

We demonstrate a controller for the half-bridge inverter that explicitly models the switches instead of making time-averaged assumptions. The controller achieves globally, asymptotically stable reference-tracking capabilities, and can handle load changes and changing inputs from a GFM control strategy. Furthermore, using a Lyapunov function to guarantee error convergence also suggests further avenues for switching policy design options. For example, a future experiment could allow a small amount of tracking error in return for reducing the switching frequency and reducing wear on the inverter switches [8]. Moreover, because we consider a single-phase system, the results found directly extrapolate to balanced three-phase systems.

In comparison with the state of the art, our proposed controller provides two significant advantages. The first is a safety guarantee. We can mathematically prove that the controller can drive the system to the desired reference signal from anywhere in the state-space. We are unaware of similar claims for the averaged model and PI controllers. A second advantage is there are no control gains that need to be tuned in this design. A significant drawback of the inner PI control loops is the reliance on its gains and the different methodologies to design them. Studies have shown how a poor choice of control gains can lead to instability [50]. Our hybrid controller avoids this tuning process altogether.

Though we believe a hybrid systems approach holds promise for further exploration, we briefly note some limitations of the inverter control design we developed here. First, our stability result relies on the ability to measure e and respond to changes in the sign of $\mathbf{B}^\top \mathbf{P} e$, which requires fast sensing and actuation. Furthermore, our stability result is so far only guaranteed for constant resistance loads, whereas most loads include constant inductance or capacitance, or even appear as elements with impedances that vary in response to source voltages. As a step toward resolving this limitation, we have shown the ability of our controller to update in real time to handle changes in resistive load, and empirically show robustness. In both of these cases, it may still be possible to provide rigorous stability guarantees after taking realistic sampling frequencies and control delays into account with further development of the theory. Moreover, ideally we would only have to rely on a sinusoidal voltage reference, as opposed to requiring a current reference as well, which is not always possible in practice. And, while we have shown simulation results for continuously changing set points, these have not yet been studied theoretically. Finally, this analysis is limited to a two-state system which we seek to extend to larger scale network-level studies. Singular perturbation theory and graph theory could prove useful tools for these analyses. We leave considering these research directions to future work.

Chapter 3

Analysis of modern power systems with high fidelity transmission line dynamics

Continuing with the objective of this theses, we now transition to addressing the the problem at hand from a transmission system perspective.

This chapter is based on the paper "Analysis of modern power systems with high fidelity transmission line dynamics" coauthored with Ruth Kravis, Sunash Sharma, Claire Tomlin, and Duncan Callaway. It has been submitted for publication and is under review at the IEEE Transactions on Power Systems Journal.

3.1 Introduction

This chapter addresses the question of whether or not electromagnetic (EM) dynamics should be included in power system wide area dynamic interaction studies as supply from converter-interfaced generation (CIG) grows in power systems. These dynamics have historically been largely ignored for studies outside of the vicinity of a disturbance due to the natural time-scale separation between synchronous machine (SM) and EM dynamics. However, because CIG operates on similar time scales as these EM dynamics [23], it is no longer clear whether fast transmission line dynamics can be neglected [19]. This question has become increasingly prominent as many researchers are calling for greater production from grid-forming (GFM) inverters that regulate voltage frequency and magnitude [45]. Furthermore, CIG can only tolerate smaller current magnitudes relative to SMs, and EM interactions could result in CIG current saturation limits being reached [23]. Moreover, the answer to this question has important computational implications: while phasor-domain modeling tools that ignore fast time-scale dynamics can simulate power system dynamics in a matter of seconds, electromagnetic transient (EMT) software tools can require many hours to simulate even relatively small systems [33].

The central component in this question which determines the difference between phasor domain simulations and EMT simulations is the transmission line (TL). Phasor-domain simulations typically have detailed load, machine, and inverter models that are coupled via algebraic line models that ignore the EM dynamics on TLs. On the other hand, EMT methods model the detailed physics of TLs – including wave propagation and frequency dependence – in tandem with other power system elements. This enables EM timescale phenomena from a variety of system components to accurately propagate from one network location to another.

Several recent studies have found that simple models of TL dynamics can impact small signal stability classifications [50, 25, 21, 59], in some situations, showing that line dynamics can destabilize grids with high shares of CIG, while stabilizing them in others. In these papers, TLs are modeled with a single RL branch [50, 21] or dynamic lumped-parameter π models [25]. While these models provide higher fidelity dynamics than algebraic models, they do not capture transmission line frequency dependence or wave propagation dynamics associated with distributed parameter or multi-segment line models. Research on HVDC (high-voltage direct-current) line models that interface with power electronic converters [12, 14, 13] has shown that frequency dependence and multiple segments can produce qualitatively different dynamics relative to single-segment frequency-independent models. This motivates studying power system dynamics with high-fidelity line models.

This paper aims to provide recommendations for the TL modeling choice in system-level dynamics and stability studies by examining the impact of TL model fidelity on simulation outcomes. In addition to comparing algebraic network models to dynamic π models, we examine multi-segment TL models with and without frequency-dependent dynamics.

In performing this research, we produce the following contributions:

- First, we develop `TLModels.jl`, an open-source Julia-based modeling package building on the open-source simulation package `PowerSimulationsDynamics.jl` [42]. This facilitates comparisons between a large variety of TL modeling choices in a single, fast-to-simulate, open-source simulation package, rather than relying on aligning simulation assumptions between commercial phasor-domain and EMT simulation software.

- Second, we examine the effect of TL model choice on the small signal stability of power systems with a mix of GFM CIG, grid following (GFL) CIG, and SMs. For the GFM-SM cases we study, increasing TL fidelity with more segments and frequency dependence alters both the real and imaginary parts of the system's eigenvalues. However, we find that the loading and line length at which systems become unstable is independent of the TL model. We further find that the additional states introduced by the higher fidelity TL models have very limited impact on the least stable eigenvalues.

- Third, we examine the effect of TL model choice on dynamic simulation outcomes for TL trips across several case studies, loading scenarios, and line lengths, for systems with a mix of GFM CIG, GFL CIG, and SMs. We observe that different line models

introduce different voltage and current dynamics, even at locations that are not adjacent to the disturbance. However, in the scenarios we study, these differences are small after 20 ms of the perturbation.

- Lastly, we recommend the dynamic π line model as a suitable model for small signal and dynamic simulation analysis for studies with time horizons longer than 20 ms after a perturbation. If a detailed analysis is required within 20 ms after a fault, the highest fidelity model is required.

Notation: Dot notation indicates the time derivative of a variable, i.e., $\dot{x} = \frac{dx}{dt}$. Bold lower-case symbols are used to represent complex variables in the dq or RI reference frames, e.g. $\boldsymbol{x} = x_R + jx_I$. $\lambda_A \in \sigma(A)$ is an eigenvalue of A, where $\sigma(A)$ is the spectrum of $A \in \mathbb{R}^{n\times n}$. $\|\cdot\|$ is the Euclidean vector norm.

3.2 Modeling

EMT and positive sequence simulations

EMT tools such as PSCAD [49] simulate systems via a sequence of coupled nodal equations in which TL dynamics and bus-level device dynamics are represented in a discrete time formulation. This allows line wave propagation dynamics and delays to be captured with high fidelity. In contrast, phasor domain tools such as PSS/e [62] and PSLF [20] solve the dynamics of devices at each bus and, in order to accelerate simulation times, represent the network model as an algebraic system solved in a separate power flow step. Phasor domain tools are further accelerated relative to EMT tools by using ordinary differential equation (ODE) solvers that numerically integrate dynamics far faster than discrete time EMT solvers [43].

These differences complicate simulation-based comparisons of dynamic phenomena with and without TL dynamics. EMT software tools are slow to solve, and significant modeling effort is required to ensure that simulation outputs without line dynamics match industry standard phasor domain modeling tools. Moreover, Bergeron-style discrete-time formulations [17] of high-frequency dynamics for TLs produce delay-*difference* equations that cannot be easily deployed in small signal stability analyses.

In this paper we leverage the Julia-based modeling and simulation package `PowerSimulationsDynamics.jl` (PSID). PSID can simulate power system dynamics in the phasor domain as well as in a balanced dq form, and it is capable of precisely reproducing the output of PSS/e in the phasor domain, even on very large network models, as well as PSCAD EMT with fast inverter and machine dynamics [42]. In contrast to PSCAD, because PSID preserves a dq ODE formulation of the system model, it can leverage a suite of numerical integration solvers that enable significantly faster simulation speeds of power system dynamics.

However, PSID only models static or dynamic π representations of TLs. In this paper we extend PSID to approximate distributed parameter TL dynamics with and without frequency dependence. We do so by adapting a multi-segment multi-branch modeling approach [4, 13] originally developed for modeling HVDC cables, to work in PSID's multi-machine AC power system simulation setting.

Power System Components

Generator

In PSID, a generator is composed of five main components: a stator, a shaft, a turbine governor, a power system stabilizer (PSS), and an automatic voltage regulator (AVR). Our choice of models for each of the components is based on the time scales over which the dynamics of the component evolves relative to the fast time scales of inverter controls and TL dynamics we are interested in.

The models that we choose for each of the components of the generator, along with the corresponding choices for parameters, can be found in Chapters 15 and 16 of [52]. We adopt the six-state Anderson-Fouad machine stator model. This model incorporates transient and subtransient EM stator dynamics. We choose a shaft model given by the swing equations with damping. Further, we opt for a fixed input turbine governor because its output will be relatively constant in the time scales of interest. Because of its use for slow timescales, and thus its irrelevance to our analysis, we choose not to include a PSS. Lastly, we choose a Type 1 AVR to capture voltage control dynamics.

Inverter

In PSID, an inverter is composed of six main components: a DC voltage source, a model for the switches, an output inverter filter, an outer GFM or GFL control loop, an inner control loop, and a frequency estimator.

The models we select for these components and their parameters come from [4]. We choose a fixed DC voltage source model, an LCL passive filter, a virtual synchronous machine (VSM) GFM model for the outer loops, nested proportional-integral (PI) loops for the inner control loops, and a phase locked loop for damping of the virtual frequency. We choose an averaged model for the switches [67]. For some experiments, we choose to have the inverter be a GFL source modeled by active and reactive power PI controllers [32].

Transmission lines

We consider TL models that accurately capture physical dynamics, and can be expressed as linear time-invariant state-space models. These are compatible with differential-algebraic equation (DAE) representations of other system components in PSID and make analysis straightforward.

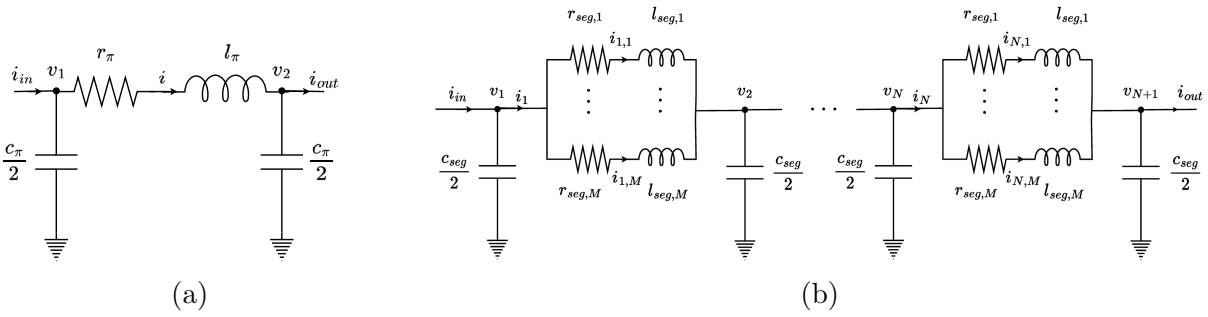

(a) (b)

Figure 3.1: Line model topologies: (a) π model (*statpi* and *dynpi*), and (b) Multi-segment model ($MSSB$ and $MSMB$).

To model TLs of arbitrary length (denoted ℓ), we use per unit length (per kilometer, or km) parameters for impedance, $z_{km} = r_{km} + jx_{km}$, and admittance, $y_{km} = g_{km} + jb_{km}$. Here, r_{km} is the resistance, $x_{km} = \omega l_{km}$ is the reactance, g_{km} is the conductance, and $b_{km} = \omega c_{km}$ is the susceptance. At a particular operating frequency ω, we compute the lumped parameter equivalent π model according to the following equations, which include hyperbolic correction factors from the steady state solution to Telegrapher's equations.

$$z_\pi = z_{km}\ell \left(\frac{\sinh(\gamma\ell)}{\gamma\ell} \right) \tag{3.1}$$

$$y_\pi = y_{km}\ell \left(\frac{\tanh(\gamma\ell/2)}{\gamma\ell/2} \right) \tag{3.2}$$

$$\gamma = \sqrt{z_{km} y_{km}} \tag{3.3}$$

Here ℓ is line length, as distinct from l which refers to inductance. We assume $g_{km} = 0$ implying that the line losses are concentrated in the RL branch and not the shunt conductance. This, however, does not imply that $g_\pi = \mathrm{Re}(y_\pi) = 0$. We choose to set $g_\pi = 0$ for the same reason. From this model, we can compute equivalent r, l, c as $r_\pi = \mathrm{Re}(z_\pi), l_\pi = x_\pi/\omega = \mathrm{Im}(z_\pi)/\omega, c_\pi = b_\pi/\omega = \mathrm{Im}(y_\pi)/\omega$, where $\omega = 2\pi f$, with f the linear frequency.

Algebraic π model (statpi)

The algebraic π model has the form shown in Fig. 3.1a. It assumes that any line dynamics are stable and settle quickly compared to other system dynamics. Therefore, the differential terms associated with the line capacitance and inductance are set to zero, giving an algebraic

model as follows:

$$\boldsymbol{i_{in}} = \left(\frac{1}{z_\pi} + y_\pi\right)\boldsymbol{v_1} - \frac{1}{z_\pi}\boldsymbol{v_2} \tag{3.4}$$

$$\boldsymbol{i_{out}} = \frac{1}{z_\pi}\boldsymbol{v_1} - \left(\frac{1}{z_\pi} + y_\pi\right)\boldsymbol{v_2} \tag{3.5}$$

Since this model is purely algebraic, any dynamics on $\boldsymbol{i_{in}}$, $\boldsymbol{i_{out}}$, $\boldsymbol{v_1}$, and $\boldsymbol{v_2}$ that arise due to the interconnection of the line with dynamic devices will instantaneously appear at the other end of the line.

Dynamic π model (dynpi)

The dynamic π model has the same topology as shown in Fig. 3.1a, but it includes dynamics on line current and voltage states:

$$\frac{l_\pi}{\omega_b}\frac{d\boldsymbol{i}}{dt} = (\boldsymbol{v_1} - \boldsymbol{v_2}) - z_\pi\boldsymbol{i} \tag{3.6}$$

$$\frac{c_\pi}{2}\frac{1}{\omega_b}\frac{d\boldsymbol{v_1}}{dt} = (\boldsymbol{i_{in}} - \boldsymbol{i}) - y_\pi\boldsymbol{v_1} \tag{3.7}$$

$$\frac{c_\pi}{2}\frac{1}{\omega_b}\frac{d\boldsymbol{v_2}}{dt} = (\boldsymbol{i} - \boldsymbol{i_{out}}) - y_\pi\boldsymbol{v_2} \tag{3.8}$$

Here ω_b is the base frequency. Similar to *statpi*, *dynpi* only captures the effect of the distributed line parameters in steady state.

Multi-segment single-branch π model ($MSSB$)

To capture the distributed nature of the line parameters in both transient and steady state responses we introduce the multi-segment models seen in Fig. 3.1b.

In what follows, a line with N multiple "segments" is one that is divided into a discrete set of identical-length π models connected in series. In addition, a line with M multiple "branches" is one in which each segment is divided into a set of parallel RL branches, each with different impedance, to capture frequency dependent line characteristics [14].

The multi-segment single branch π model ($MSSB$) consists of N π-shaped segments. The parameters for each segment are given by:

$$r_{seg} = r_{km}\ell_{seg} \tag{3.9}$$

$$l_{seg} = l_{km}\ell_{seg} \tag{3.10}$$

$$c_{seg} = c_{km}\ell_{seg} \tag{3.11}$$

where $\ell_{seg} = \frac{\ell}{N}$ is the segment length. Further, $z_{seg} = r_{seg} + j\omega l_{seg}$ and $y_{seg} = j\omega c_{seg}$. This model is seen in Fig. 3.1b when choosing $M = 1$, namely a single RL branch for

each segment. The i^{th} segment of an N-segment $MSSB$ model is defined by the following equations:

$$\frac{l_{seg}}{\omega_b}\frac{d\boldsymbol{i_i}}{dt} = (\boldsymbol{v_i} - \boldsymbol{v_{i+1}}) - z_{seg}\boldsymbol{i_i} \tag{3.12}$$

$$\frac{c_{seg}}{2}\frac{1}{\omega_b}\frac{d\boldsymbol{v_i}}{dt} = (\boldsymbol{i_{i-1}} - \boldsymbol{i_i}) - y_{seg}\boldsymbol{v_i} \tag{3.13}$$

$$\frac{c_{seg}}{2}\frac{1}{\omega_b}\frac{d\boldsymbol{v_{i+1}}}{dt} = (\boldsymbol{i_i} - \boldsymbol{i_{i+1}}) - y_{seg}\boldsymbol{v_{i+1}} \tag{3.14}$$

Note that $\boldsymbol{i_0} = \boldsymbol{i_{in}}$, and $\boldsymbol{i_{N+1}} = \boldsymbol{i_{out}}$. As N is increased, the $MSSB$ model more closely approximates the equivalent π model in steady state frequency response.

Frequency dependent multi-segment multi-branch π model ($MSMB$)

The $MSMB$ model has M branch currents per segment, as seen in Fig. 3.1b. Let the subscript $m = 1, ..., M$ denote the m^{th} parallel branch. Therefore, the equations for the i^{th} segment are:

$$\frac{l_{seg,m}}{\omega_b}\frac{d\boldsymbol{i_{i,m}}}{dt} = (\boldsymbol{v_i} - \boldsymbol{v_{i+1}}) - z_{seg,m}\boldsymbol{i_{i,m}} \quad \forall m \tag{3.15}$$

$$\frac{c_{seg}}{2}\frac{1}{\omega_b}\frac{d\boldsymbol{v_i}}{dt} = (\boldsymbol{i_{i-1}} - \boldsymbol{i_i}) - y_{seg}\boldsymbol{v_i} \tag{3.16}$$

$$\frac{c_{seg}}{2}\frac{1}{\omega_b}\frac{d\boldsymbol{v_{i+1}}}{dt} = (\boldsymbol{i_i} - \boldsymbol{i_{i+1}}) - y_{seg}\boldsymbol{v_{i+1}} \tag{3.17}$$

where $z_{seg,m} = r_{seg,m} + j\omega l_{seg,m}$. Note that $\boldsymbol{i_i} = \sum_{m=1}^{M} \boldsymbol{i_{i,m}}$ in the voltage equations.

The $MSMB$ is considered the highest fidelity line model of those presented since it captures dynamics along the line's length as well as the additional damping that arises due to the frequency dependence of the line parameters [13].

Line parameters

For the $MSMB$ model, we obtain $r_{km,m}$, $l_{km,m}$, and c_{km} for each branch from known line data via vector fitting [22, 4], a form of parameter estimation based on real transmission line data. In this paper, we use the frequency dependent line impedance parameters from [17] as a starting point[1]. While the data set is realistic, the number of samples is limited. We acknowledge this and keep this in mind when performing the analysis.

We derive parameters for all other line models from the $MSMB$ model by finding the equivalent parallelized branch impedance at nominal frequency for the $MSMB$ model. This yields the $MSSB$ z_{km}, which we use in Equations 3.1, 3.2 and 3.3 to obtain the lumped

[1]We use the data in Table 3 of [17].

model parameters for *statpi* and *dynpi*. Following this procedure ensures that at the steady-state operating frequency, all line models have the same impedance and so result in the same network power flow solution.

Aggregate system model

All the models described above can be written into a DAE form for the entire network under study. Linking the devices and network, we arrive at a mathematical form as follows:

$$\begin{bmatrix} \dot{x} \\ 0 \end{bmatrix} = \begin{bmatrix} f(x, y, u) \\ g(x, y, u) \end{bmatrix} \tag{3.18}$$

Here, $x \in \mathbb{R}^n$ are the system's dynamic states, $y \in \mathbb{R}^m$ are the system's algebraic states, $u \in \mathbb{R}^p$ are the system inputs. $f : \mathbb{R}^n \times \mathbb{R}^m \times \mathbb{R}^p \to \mathbb{R}^n$ and $g : \mathbb{R}^n \times \mathbb{R}^m \times \mathbb{R}^p \to \mathbb{R}^m$ are the vector equations associated to the dynamics of the network and the algebraic constraints.

In general, f is a nonlinear vector field. Therefore, to study the small signal stability of the system we find an equilibrium point $(x^\star, y^\star, 0)$ by setting $\dot{x} = 0$ and solving the nonlinear system of equations. We linearize them around that point, and arrive at a set of linear dynamics that characterize the behavior of the system in the vicinity of that equilibrium point. The resulting equations will then be of the following form:

$$\dot{\Delta x} = J(x^\star, y^\star)\Delta x \tag{3.19}$$

Here, $J(x^\star, y^\star) \in \mathbb{R}^{n \times n}$ is the reduced system Jacobian matrix. By studying the eigenvalues of this matrix, we can determine if $(x^\star, y^\star, 0)$ is a stable or unstable operating condition for the network. See [25] or [42] for further details on the linearization process in PSID.

3.3 Test Cases

To investigate dynamic interactions under the different line models presented, we choose a simplified Two Bus test case and the IEEE WSCC 9 Bus test case as representative models of how we could expect a power system to behave.

Remark. *We choose not to use an infinite bus in any of our studies because it would instantaneously produce or consume whatever real and reactive power are necessary to maintain its voltage, which has an unrealistic effect on the dynamic results. Instead, we choose a SM (synchronous machine) or GFM inverter as the voltage angle reference bus to solve the initializing power flow problem and subsequently simulate dynamics of the system.*

Two Bus test case

The Two Bus test case, shown in Fig. 3.2, has two generation sources connected by two identical transmission lines in parallel. By default, $\ell = 100$ km. The test case has a constant

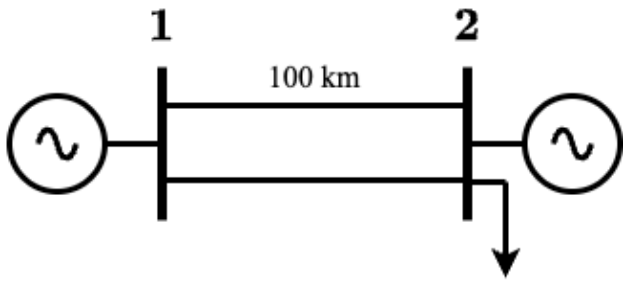

Figure 3.2: Two Bus test case single line diagram.

Case	Bus 1	Bus 2
1	SM	SM
2	SM	GFM
3	GFM	SM
4	GFM	GFM

Table 3.1: Generator configurations for the Two Bus test case.

impedance load, and we can choose its location. We choose p_{load} and q_{load} according to the line's surge impedance loading $(SIL) = \frac{V^2}{Z_c}$, where V is the nominal system voltage (230 kV) and $Z_c = \sqrt{z_{km}/y_{km}}$ is the line's characteristic impedance. Normally, SIL is computed for lossless lines; however, here we consider losses to obtain nominal SIL values for real and reactive power. For our parameters of V, z_{km}, and y_{km}, we arrive at $p_{load} = 2.05$ p.u. and $q_{load} = 0.08$ p.u.

We choose either a VSM GFM or SM for each of the two buses, resulting in the cases outlined in Table 3.1. We choose not to have a GFL under the hypothesis that we need strong voltage support for a two bus network.

IEEE WSCC 9 Bus test case

We also study the IEEE WSCC 9 Bus test case, shown in Fig. 3.3. The test case includes three generation sources at buses 1, 2, and 3, and three constant impedance loads at buses 5, 6 and 8. We set nominal loading and line lengths according to [5].

Generator configurations are shown in Table 3.2. These scenarios were selected based on what we understand to be representative of the present-day grid, and a few cases of what we anticipate the grid could look like in the future.

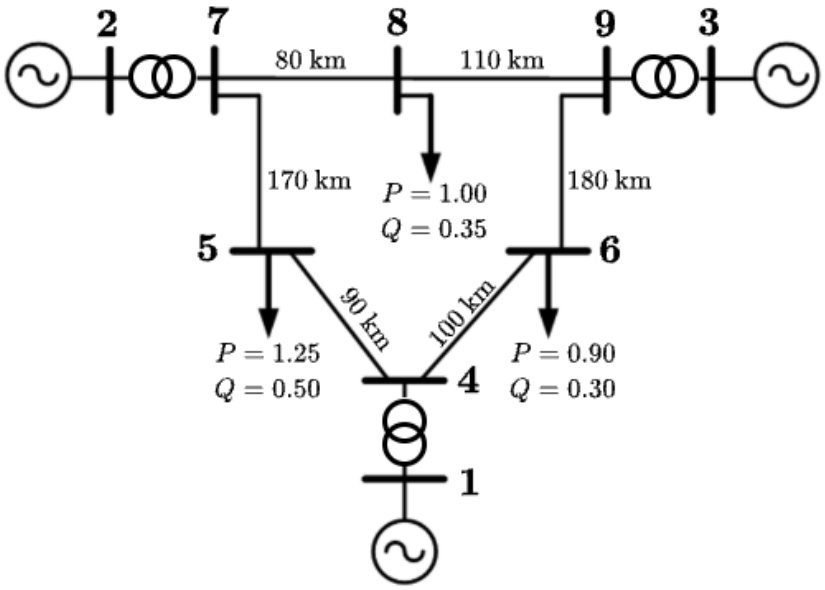

Figure 3.3: IEEE WSCC 9 Bus test case single line diagram [63].

Case	Bus 1	Bus 2	Bus 3
1	SM	SM	GFL
2	SM	GFL	GFL
3	SM	GFM	GFL
4	SM	SM	GFM
5	SM	GFM	GFM
6	GFM	SM	GFM

Table 3.2: Generator configurations for the IEEE WSCC 9 Bus test case.

Experiment types

We use `PowerSystemsExperiments.jl` (PSE), a software package capable of implementing multidimensional parameter sweeps, parallelizing hundreds of PSID simulations to accelerate simulation time and capabilities, and produce interactive plots.

All of our results can be reproduced by running code in our publicly available GitHub repository: https://github.com/Energy-MAC/EffectsOfTLDynamics.

We construct different experiments by varying the network loading, line lengths, and generator configuration. We vary loading because it is a key variable of interest for a system operator identifying safe operating limits of a system. We vary line lengths under the hypothesis that differences between line models may be revealed only for longer lines. We choose different generation configurations to study if the line model effect depends on the generation configuration.

We vary all loads' real and reactive power consumption by multiplying nominal values by a *load scale* factor, and we scale all generators' real and reactive power setpoints correspondingly. We vary line length by scaling all nominal line lengths by a *line scale* factor.

Because the $MSMB$ model attempts to capture the physics as realistically as possible, and it was fit using real TL data, we consider results obtained from $MSMB$ as the benchmark. For the $MSMB$ model we choose three parallel branches (i.e., $M = 3$), which is consistent with the modeling recommendations in [13], and N to result in 10 km line segments for both $MSSB$ and $MSMB$.

Lastly, while we choose realistic parameter and gain values for the whole network, and hypothesize that the conclusions here could be extrapolated to other power system test cases, we acknowledge that our conclusions are valid for the parameter choices we select. Further results across other parameter dimensions can be found in [39].

3.4 Small signal analysis

We compare small signal stability under our four different line models and provide results for the different test cases.

Two Bus test case

Stability boundary

Fig. 3.4 shows the line length on the y axis, using *line scale* as a direct measure, at which an eigenvalue of the linearized system crosses the imaginary axis under a range of loading conditions on the x axis. That is, line lengths below these traces are stable operating conditions, and on or above them are unstable. Four traces are plotted, one for each line model. The stability 'boundary' was calculated using increments of 0.1 *line scale*, which correspond to 10 km increments given that the nominal length is 100 km.

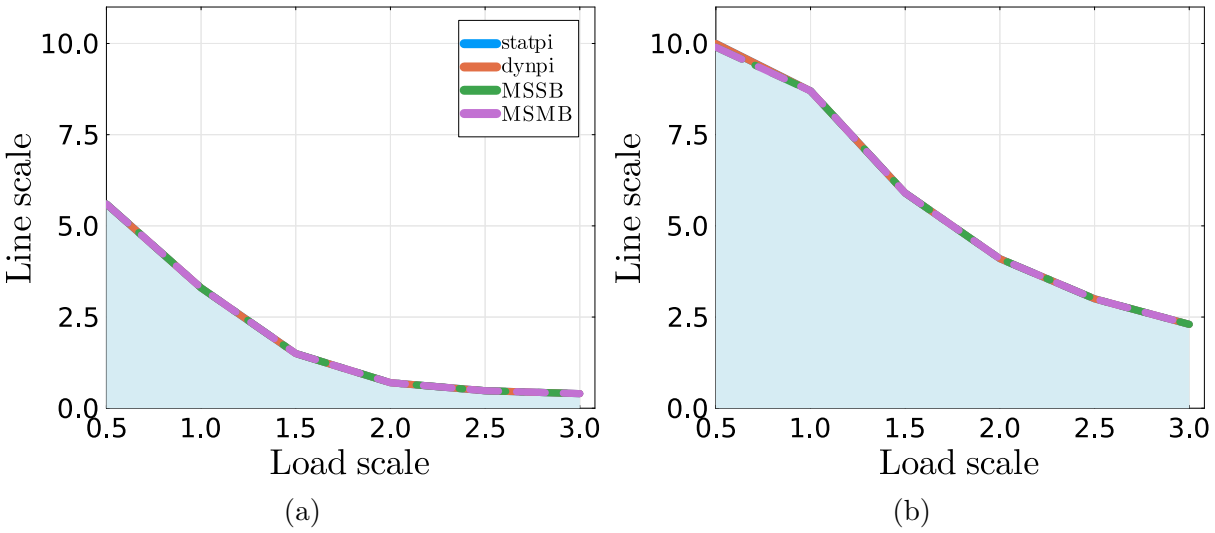

Figure 3.4: Line length where the system loses stability on the y axis (measured in terms of *line scale*) versus system loading on the x axis (measured in terms of *load scale*) for the Two Bus test case. Subfigure (a): case 3 in Table 3.1 (GFM SM) with the load at the Bus 1. Subfigure (b) is case 4 in Table 3.1 (GFM GFM) with load at Bus 2.

Fig. 3.4 demonstrates that all line models produce nearly identical predictions of the line length at which instability arises across this broad range of line lengths and loading conditions. The only perceptible differences in the stability boundary are at very long lengths (line scale of 10); we consider this to be a relatively weak result because these lengths are rare in practice and the stability boundaries are very similar.

Considering the similarity between $MSSB$ and $MSMB$ results in the range of parameters we studied, we conclude that the extra fidelity of the $MSMB$ model does not affect the least stable eigenvalues for this system. We would like to emphasize this is true even for Case 4 in Table 3.1, in which all the generation comes from GFM CIG. This implies that, in the cases we study, the interactions of high fidelity line model dynamics with the fast controls of inverters do not produce new unstable modes.

These results are different from other GFM-SM simulations [50] which found that the stability boundaries differ for algebraic versus dynamic π models. These differences, however, can be attributed to sweeping parameters in different dimensions: while here we sweep line lengths and loading conditions, other results sweep percentage of CIG. Their result is also in alignment with the results in [39], which also concludes that percentage of CIG impacts small signal stability conclusions for different line models.

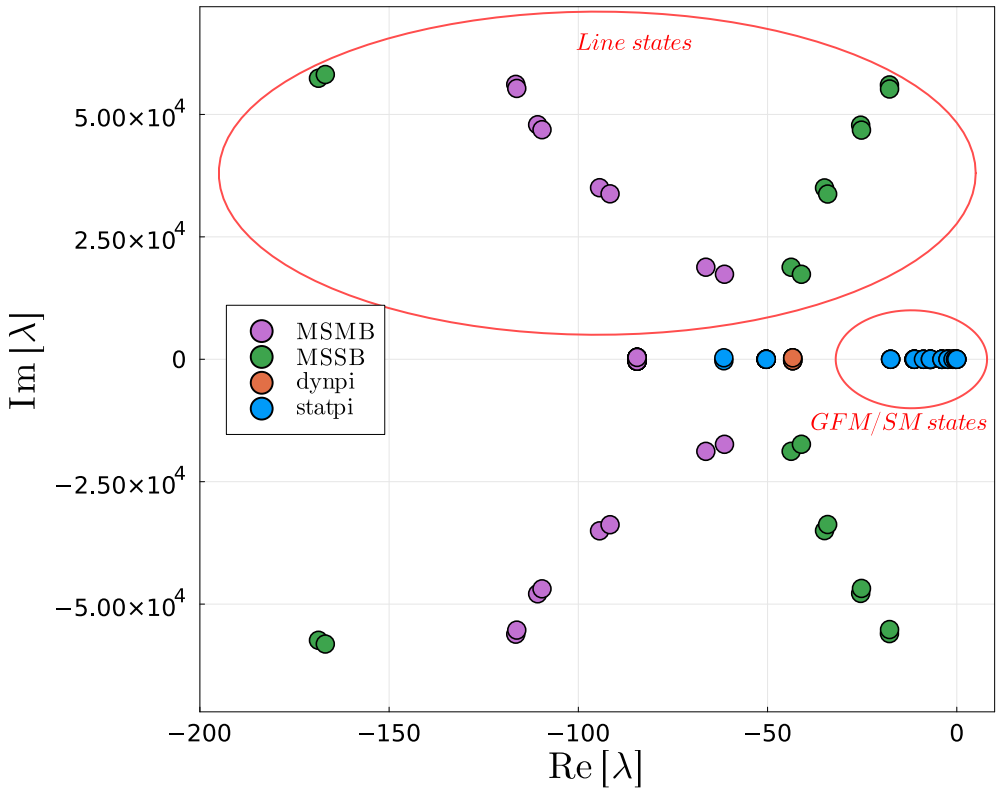

Figure 3.5: System eigenvalues under different line models in the Two Bus test case, for case 3 in Table 3.1 (GFM SM), with the load at Bus 1, and *load scale* = 1.0, *line scale* = 1.0.

Eigenvalue analysis

Fig. 3.5 compares the system eigenvalues under different choices of line models for a system with nominal loading and line scaling. The blue cluster of least stable eigenvalues near the $j\omega$-axis are common to all line models (i.e., in the image, orange, green and purple markers all lie beneath the blue symbol), and the orange eigenvalues are common to all models except *statpi*. The green markers correspond to only $MSSB$, and purple symbols correspond to only $MSMB$.

$MSSB$ (green) and $MSMB$ (purple) models exhibit higher frequency eigenvalues compared to *dynpi*, and the $MSMB$ (purple) high frequency eigenvalues are more damped compared to the $MSSB$ (green) eigenvalues. However, the least stable eigenvalues, in blue, have very low ($< 1e{-}4$) participation from line states. This supports our finding that added line fidelity does not influence small signal stability for the cases we studied. The high frequency eigenvalues are almost exclusively associated with internal line states.

In Fig. 3.6 we plot how system eigenvalues move in the complex plane under changing line lengths (Fig. 3.6a) and loading (Fig. 3.6b) for the $MSMB$ model. Since we chose 10 km

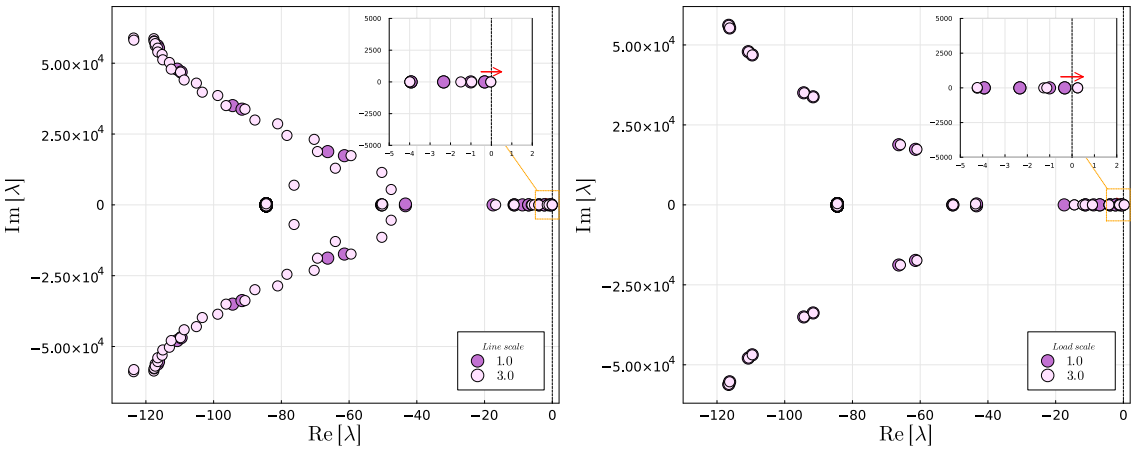

(a) (b)

Figure 3.6: $MSMB$ eigenvalues for the Two Bus test case for case 3 in Table 3.1 (GFM SM) under a variation of (a) line lengths (with *load scale* = 1.0) and (b) loading (with *line scale* = 1.0).

line segments, increasing the line lengths results in more segments, and thus more line states and eigenvalues. Therefore, a one-to-one comparison of eigenvalues for different line lengths is not possible. However, while more eigenvalues are present for longer lines, we observe that the high frequency eigenvalues which have more participation from line states are fairly similarly located for both cases. Eigenvalues closer to the imaginary axis may move right as line and loading increase, and in some cases even result in a small signal unstable operating condition, also seen in the figure.

In Fig. 3.6b, we see that that the high frequency line eigenvalues are very weakly influenced by loading, and instability again arises due to the cluster of common eigenvalues approaching the RHP (right-half plane).

3.5 Dynamic simulations

In this section, we run time domain simulations of the test cases to see how they respond to disturbances. We first justify the variables that we pay close attention to, then we discuss and justify the perturbation we apply to the systems, and finally we present the results of our dynamic studies.

Variables, disturbance, and parameters of interest

In this section, we will assess the influence of line models on the dynamic behavior of inverter currents. This is often studied with static line models on the grounds that electromagnetic

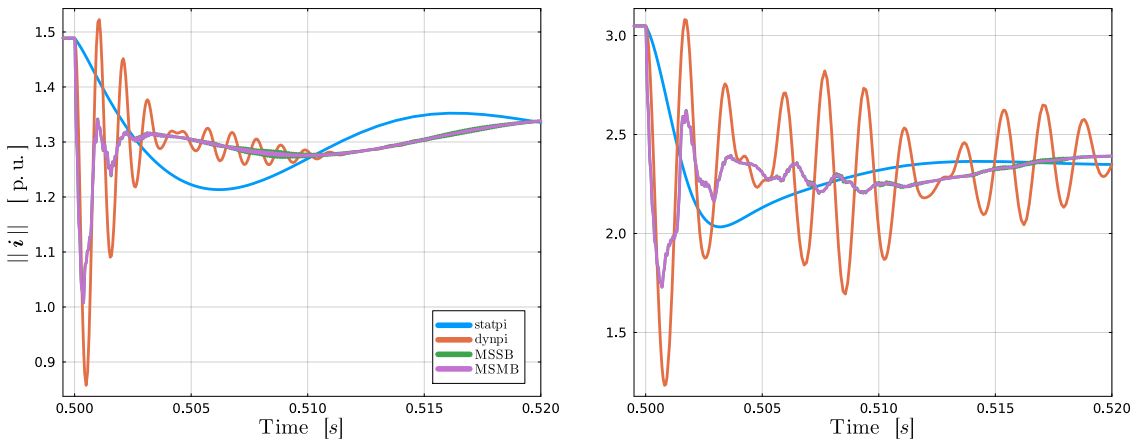

(a) (b)

Figure 3.7: Inverter current magnitude at Bus 2 for case 2 in Table 3.1 for the Two Bus test case with a branch trip. The *line* and *load scale* are 1.0, 1.0 in subfigure (a). The *line* and *load scale* are 2.0, 2.0 in subfigure (b).

transients will dissipate faster than the dynamics that govern overall stability phenomena. However, as CIG infeed increases, there is less certainty on the validity of this assumption.

Inverters are known to tolerate up to $\sim$ 1.3 p.u. (on the device base) rated current without risking damage to device switches. Therefore, we will focus our attention on the current at inverter filters to identify whether low fidelity line models could fail to identify high inverter current magnitudes. Since we consider different cases according to Tables 3.1 and 3.2, we study the current of the generating device at each bus. In the case of an inverter, we measure the inductor filter current, and in the case of a machine, we measure the stator current. We show current measurements in per unit relative to the system base. Note that PSID does not currently model a current saturation block to protect switches from overcurrent. Therefore, our simulation results can be used to identify events in which overcurrent protection could be activated, but are not indicative of the dynamics that would ensue following an overcurrent event.

We perturb the system with a TL trip because it affects the system abruptly and directly excites the line dynamics. As in the small signal analysis above, we test the system under a range of loading, generator configuration, and line length scenarios. The generator configuration is unique to each test case in Tables 3.1 and 3.2. We choose *line scale* $\in \{1.0, 1.5, 2.0, 2.5, 3.0\}$ to study normal and long TL lengths and *load scale* $\in \{0.5, 1.0, 1.5, 2.0\}$ to study systems with low, medium, and high loading for both test cases. We perform simulations with all combinations of these parameter values for all line models, resulting in several hundred simulations. Due to lack of space, we only choose representative examples of larger trends in the results to showcase here.

Two Bus test case

We present results for the Two Bus test case for Case 2 in Table 3.1, with a SM at Bus 1 and GFM at Bus 2. The load is kept at Bus 2 for all simulations. We trip one of the lines since they are identical and will have the same loading.

Fig. 3.7 shows the current magnitude at Bus 2 for this simulation. We show results for the 20 ms time window after the disturbance is applied because the dynamics of all line models converge to practically the same trajectory after approximately this time. We find that the line models produce qualitatively different dynamics following a TL trip as expected: oscillations are present for all line models, with increasing frequency oscillations present for increasing modeling fidelity. However, $MSSB$ and $MSMB$ produce nearly identical dynamics, suggesting that modeling line frequency dependence with $MSMB$ may not be necessary for studies on this time scale. *Statpi* does not reflect the oscillations present in $MSMB$.

The *dynpi* line model consistently shows two behaviors: first, its maximum (minimum) value for current magnitude is generally larger (smaller) than all other line models; second, it shows some low-frequency oscillations of larger amplitude relative to other line models. We refer to this as *dynpi enveloping* the other line model dynamics. We therefore conclude that *dynpi* is a conservative estimate relative to our benchmark dynamics given by $MSMB$.

IEEE WSCC 9 Bus test case

For the IEEE WSCC 9 Bus test case, we studied current injections into the network at all three generator buses. We trip the heaviest loaded line in the network which connects buses 5 and 7 because it is the heaviest disturbance that we could apply and we hypothesize that differences from line models could be revealed in such a case. For some experiments, we alternatively trip the line connecting buses 4 and 5, which is the second heaviest loaded line.

We pay particularly close attention to (and only show results for) the generator at Bus 2 because it is the one closest to the disturbance. We show the first 20 ms after the fault as for the Two Bus case for the same reason.

Effect of generator portfolio

Fig. 3.8 shows the current magnitude at Bus 2 for *line scale* and *load scale* values of 1.0, and cases 2, 3, and 5 in Table 3.2. Again, all line models converge to the same behavior closely after the 20 ms presented in the plots, whether or not the eventual dynamics are stable or unstable.

We find similar results to the Two Bus test case: $MSSB$ behavior is nearly identical to $MSMB$, and *dynpi* envelopes other line model behavior. *Statpi*, moreover, significantly underestimates oscillations and maximum and minimum peak values.

Though line models did not introduce differences in long term dynamics for different generator configurations, we did find that generator configuration plays a role in system

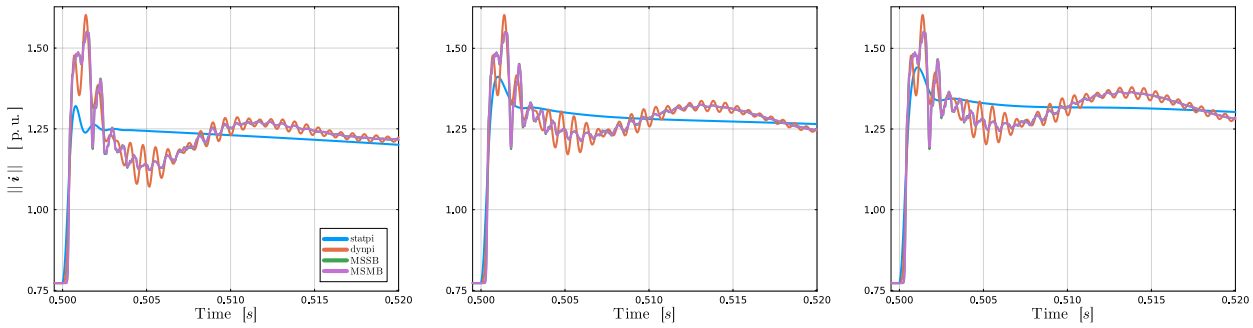

(a) (b) (c)

Figure 3.8: Sub (a), (b), and (c) show inverter current magnitude at Bus 2 for the following generation configurations: SM GFL GFL, SM GFM GFL, SM GFM GFM (cases 2, 3, and 5 in Table 3.2) respectively for the IEEE WSCC 9 Bus test case. *line scale* and *load scale* are both 1.0.

stability (results not shown), consistent with prior work [50]. Specifically, we found that networks with mostly SMs or GFM inverters – implying more voltage and frequency control – settle to a new stable equilibrium point after a disturbance when *line scale* and *load scale* are low. Cases with GFL inverters destabilized significantly more easily.

Effect of line length

Fig. 3.9 shows the current magnitude at Bus 2 for *load scale* = 1.0 for case 3 in Table 3.2, and varying *line scale*, which is representative of the results found. As with our experiments for generator configuration, for a given line length all line models generated similar dynamic behavior beyond the 20 ms time window shown in Fig. 3.9. The higher fidelity models showed a delayed effect on current response, which is more evident for longer lines. *Dynpi* showed a smaller delay, and *statpi* showed no delay. This can be attributed to the energy storage introduced by modeled line capacitance and inductance. As one would expect, current at buses further from the disturbance show a greater delay (result not shown). While these delays are followed by short term differences in current dynamics across different line models, we did not observe long term differences between dynamics introduced by different line models.

As with the generator portfolio results above, $MSSB$ dynamics are nearly identical to $MSMB$, *dynpi* envelopes other line model behaviors, and *statpi* over-simplifies much of the behavior.

For very long lines (e.g. *line scale* = 3.0, equivalent to line lengths well above 300 km in this network), we found that the multi-segment models produce a slightly higher peak than *dynpi*, as seen in Fig. 3.9c.

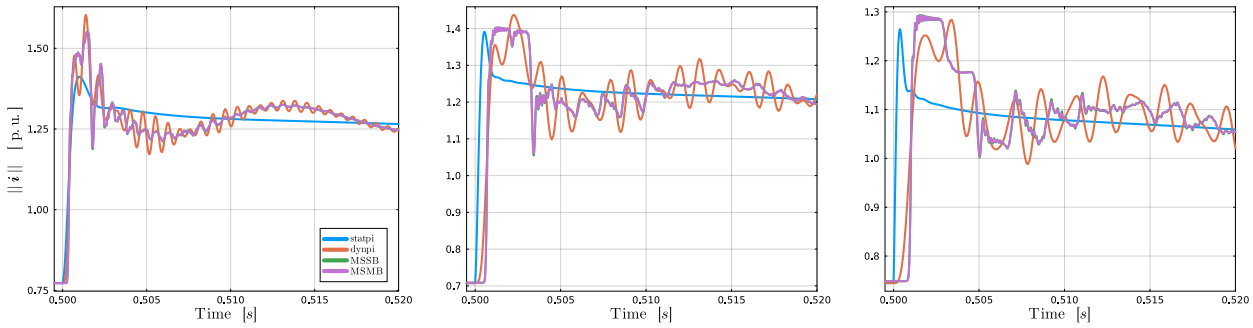

(a) (b) (c)

Figure 3.9: Inverter current magnitude at Bus 2 for the SM, GFM, GFL configuration (case 3 in Table 3.2) for the IEEE WSCC 9 Bus test case, and *load scale* = 1.0. *Line scale* varies: 1.0, 2.0, 3.0 in sub (a), (b), and (c) respectively.

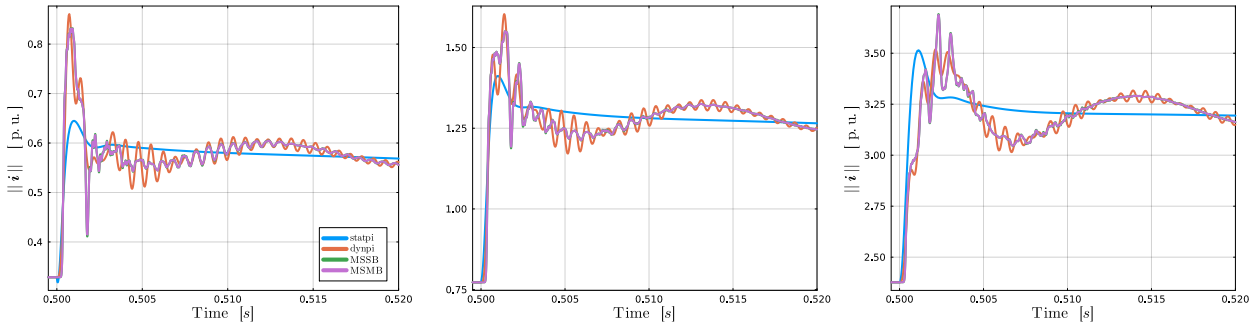

(a) (b) (c)

Figure 3.10: Inverter current magnitude at Bus 2 for SM, GFM, GFL configuration (case 3 in Table 3.2) for the IEEE WSCC 9 Bus test case, and *line scale* = 1.0. *Load scale* varies: 0.5, 1.0, 2.0 in sub (a), (b), and (c) respectively.

Effect of loading

Fig. 3.10 shows the current magnitude at Bus 2 for case 3 in Table 3.2 with varying *load scale* and *line scale* = 1.0. Again, outside of the simulation window shown here, the dynamics converge to the same behavior for all line models.

We found consistent results with other parameter sweeps: $MSMB$ and $MSSB$ produce practically identical dynamics, *dynpi* enveloped other line dynamics, and *statpi* simplifies much of the behavior. We also see that, similar to the effect of long lines, at heavy loading (e.g., Fig. 3.10c) the $MSMB$ model produces a slightly higher peak than *dynpi*. However, none of these cases show any evidence that the line model significantly affects the dynamic behavior at different loading levels.

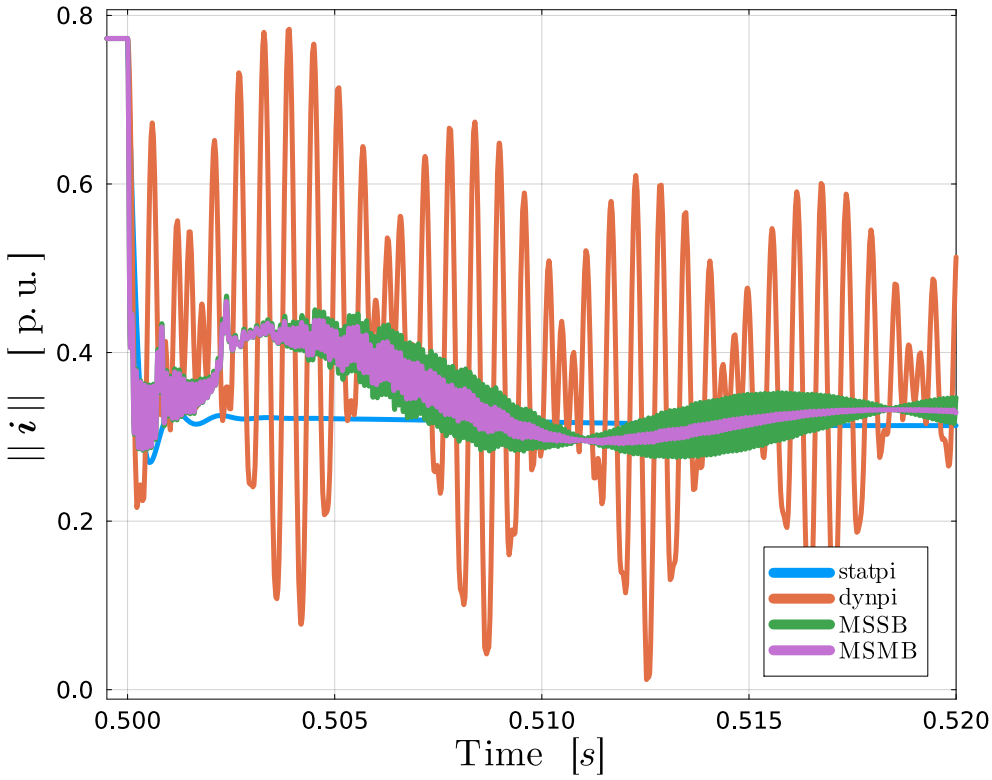

Figure 3.11: Current magnitude at Bus 2 for the IEEE WSCC 9 Bus test case for SM GFL GFL generation configuration (case 2 in Table 3.2). *line scale* and *load scale* are both 1.0 for a TL trip of the line connecting Buses 4 and 5.

Tripping Line 4-5

We also tripped the line connecting Bus 4 and 5, which is loaded at about 70% of the line between Bus 5 and 7. This places the fault further away from the location of current measurement at Bus 2.

Fig. 3.11 shows the current magnitude at Bus 2 for *line scale* and *load scale* values of 1.0, and case 2 in Table 3.2. As with the results above, the *dynpi* amplitude is greater than other line model dynamics. However, the effect is significantly more noticeable under this scenario: there exists a lower-frequency, high-amplitude signal in the *dynpi* behavior that is not present for $MSMB$. We found this behavior to be consistent across the *line scale*, *load scale*, and generator configuration parameter sweeps we performed for this perturbation. Moreover, $MSSB$ and $MSMB$, while similar, do not completely overlap as is the case in all previous scenarios. All line model behaviors still eventually converged to similar behavior.

Discussion

In this section we discuss and synthesize results across all categories of dynamic simulations to produce generalized observations about line model performance.

The fact that $MSSB$ and $MSMB$ almost always show the same transient behavior for current magnitude, as seen in Figs. 3.7–3.10, suggests that the additional modeling complexity of $MSMB$ relative to $MSSB$ is generally not necessary for wide area transient dynamic simulations.

Further relative to all other line models, *statpi* consistently underestimates the peak values and amplitudes of oscillations see Figs. 3.7–3.11. This is particularly important for modeling inverter current saturation blocks.

In contrast to *statpi*, we find that *dynpi* tends to *overestimate* amplitudes relative to $MSMB$, as in Figs. 3.7, 3.8, 3.9, 3.10. In some cases, this can be by a large amount, such as in Fig. 3.11.

Moreover, *statpi* produces the least amount of high frequency oscillations, *dynpi* generates some oscilations, and $MSSB/MSMB$ show the most. This aligns with our expectations because higher-fidelity models increase the line's bandwidth, suggesting that signals of higher frequency propagate more easily. While the currents from $MSSB/MSMB$ simulations show higher frequency components than those of *dynpi* simulations, these typically have small amplitude, and decay quickly.

It is important to recall, as seen in Figs. 3.9c and 3.10c, that under particularly long lines, or under particularly heavy loading conditions, the *dynpi* model may not be able to precisely capture peak values.

Finally, the *statpi* error relative to $MSMB$ is greater at buses with GFL than at buses with GFM, as seen in Fig. 3.8a vs. Fig. 3.8b. *Statpi* also showed more error in cases with lighter loading, as seen in Figs. 3.7, 3.10a and 3.10b.

3.6 Conclusions and recommendations

We develop `TLModels.jl` as an open-source modeling software for TL modeling of varying fidelity. Using this tool, we perform detailed dynamic simulations and small signal analyses of power systems.

For the small signal analysis, we find that each line model generates different sets of eigenvalues. However, for the cases we investigated, the dynamic line states have very low participation factors in the least stable eigenvalues and do not impact stability conclusions. Therefore, we conclude that line model fidelity does not alter small signal stability conclusions under the different network conditions that we studied. Indeed, other papers have found that simple line dynamics impact the range of converter gain parameters that result in a stable operating condition [25], and that conclusions may differ with generator portfolio [50], GFM devices using virtual oscillator control [21], and even percentage of generation in the form of CIG. This is partially addressed in [39] and merits further investigation.

Dynamic simulation results show that *dynpi* envelopes and overapproximates the current trajectories produced by the $MSMB$ model while *statpi* consistently underapproximates them for the range of parameter sweeps considered. We therefore conclude that *dynpi* manifests conservative dynamics while *statpi* manifests oversimplified dynamics. $MSMB$ almost always behaves identically to $MSMB$. Therefore we recommend initial dynamic investigations to be performed with the *dynpi* model. In case a current saturation limit is observed with the *dynpi* model, for example, then a more detailed study with the $MSMB$ model would be warranted. If particularly long lines or particularly heavy loading conditions are of interest to study for the first 20 ms following a perturbation, the $MSMB$ model will be necessary. These recommendations offer a tradeoff between modeling complexity and computational burden.

Future work includes performing further tests on the IEEE WSCC 9 Bus test case with different levels of CIG penetration and power injections. Further, we would like to study larger test cases such as the 54 Bus Southeast Australian network. While we performed a multi dimensional parameter sweep and hypothesize these types of results will hold, there are still other parameter dimensions to be explored, and larger test systems have more complex and realistic dynamic interactions and merit further study.

Chapter 4

Analysis of modern power systems with high fidelity load dynamics: Introducing ZIP-E loads

After discussing contributions at the generation level in Chapter 2, and the transmission level in Chapter 3, we now focus our attention on load modeling for modern power system analysis.

This chapter is based on the paper "Analysis of modern power systems with high fidelity load dynamics: Introducing ZIP-E loads" presented at the 2024 North American Power Symposium in Austin, Texas. It was coauthored with Reid Dye, Claire Tomlin, and Duncan Callaway.

4.1 Introduction

This chapter aims to study the impact of load modeling in power grids with high penetrations of power electronics converters. Among power systems components, loads have not seen many widely adopted models for transmission system simulation compared to generators, and transmission lines [51, 47, 40, 56, 10]. This can be attributed to several reasons, one of which is the inherent challenge of modeling loads: power consumption is a function of many conditions, including weather, time of day, geographic location, and even human behavior. Therefore, most of the analysis done for power system stability has been using a select few model options

Data centers, electric vehicle superchargers, large-scale battery storage, and variable frequency drives (VFDs) are examples of power electronic loads connecting on the grid, and available load models do not accurately capture their dynamics for all time scales. Moreover, any analysis is limited in scope to the results produced from the choices of models. Therefore, there exists a need for power systems analyses with models that represent loads being connected on the grid.

A survey on power system industry members in 1988 [11] found that the most common load modeling practice was constant current loads for active power loads and constant impedance loads for reactive power loads. ZIP loads, static linear combinations of constant impedance, constant current, and constant power loads, were also common, and only a small number of industry members used dynamic load models.

Another survey in 2013 [54] found that there was no industry standard for load models and that this choice varied significantly by continent. Variations of static ZIP loads, however, were the most common model, constituting 70% of industry load models worldwide. Another common practice in the study was converting a ZIP load into an equivalent exponential model with a non-integer exponent. The survey also found that it is a common practice in the United States of America to use a composite load model incorporating both a static load component in the form of a ZIP load and a dynamic load component (typically an induction motor) in parallel.

Other load models have been proposed to capture a load's dependence on frequency. These usually take the form of a linear combination of two ZIP load models [11]. A similar attempt is made by the EPRI LOADSYN and ETMSP static load models [11]. These, however, according to the surveys, were not widely adopted by industry members.

Despite the 25 year gap between the surveys, the most recent does not show significant changes in the way industry models loads despite the increasing level of power electronics loads on the grid. This further means that corresponding analyses have not had accurate representations for power electronic loads.

In 2022, the IEEE Standards Association and IEEE Power and Energy Society published a guide for load modeling for simulations of power systems [30]. The guide acknowledges that only a few load models are widely accepted among industry members. For dynamic loads, motors are the most common model [46], and the exponential recovery load model captures aggreagate transmission-level load dynamics [27].

Lastly, the state-of-the-art load model for phasor domain simulations is the WECC composite load model [37] but is limited to static models for power electronic loads, except for VFDs [55]. It, however, does not represent inverter control loops relevant for higher frequency dynamics. A recent paper [24] uses dynamic power electronic load models for EMT studies with line dynamics but assumes no load heterogeneity.

In sum, loads are typically modeled as static ZIP loads, with motors seldom incorporated for dynamic simulations. Further, there is no well-motivated way of choosing how a load is modeled for different kinds of studies. This suggests for the last 40+ years industry has largely been using the same models for EMT and small signal analysis.

It has been posited that power electronic loads need to be modeled as constant power loads for analysis [30], however, this static model choice is an approximation of a dynamic device. Therefore, while this may be an accurate modeling choice for slow time scales, we believe we should model power electronics load with corresponding dynamics for analysis on fast time scales. This is further motivated by concerns regarding current saturation limits for inverters [53] and how this affects stability conclusions and inverter current dynamics.

So, there is a gap in the literature for analysis of power systems with models that represent the new devices being connected.

Therefore, in this chapter we introduce ZIP-E loads, a composite load model including a static ZIP model, and a power electronic load, which we denote as an E load, for the analysis of power systems with power electronic loads. We model this load as a grid-following (GFL) inverter that consumes instead of delivers power: it operates as a rectifier, as are the the power electronic loads described. An E load is meant to capture the dynamics of those power electronic devices, and the ZIP-E load is meant to capture heterogeneity in the load profile.

For now, we do not incorporate motors as loads for two primary reasons: i.) we seek to identify the modeling impact of changing P loads to E loads, and ii.) most modern motor loads are interfaced with VFDs, which inherently have a power electronics interface of the form we choose to model here.

To our knowledge, this is the first small signal and EMT study of power systems with heterogeneous load models that includes physics-based models for power electronic loads.

We believe that ZIP-E loads provide a flexible alternative for load modeling during fast time scales: ZIP-E loads adopt i.) the common industry practice of ZIP loads, ii.) the notion that power electronic loads will behave as constant power loads in steady state, iii.) an energy buffer so the constant power constraint of the load is relaxed during transient events, and iv.) a physical representation of power electronic loads capturing the dynamics of new loads being incorporated into the grid.

Further, by modeling loads in this way we consider fast dynamics on both generation and load, meaning that fast line dynamics could be relevant. We investigate their effect as well.

This research is guided by the following questions:

- What, if any, qualitative differences are there between the conclusions of small signal stability analyses of power systems that use ZIP versus ZIP-E load models?
- Can ZIP-E loads influence inverter current dynamics in ways not otherwise manifested by ZIP models?

This chapter's contributions are:

- `ZIPE_loads.jl` – A Julia-based open source modeling package for ZIP-E loads extending the modeling and simulation capabilities of `PowerSimulationsDynamics.jl` [41].
- An analysis of load model effects on small-signal and transient stability of the IEEE WSCC 9 Bus Test Case.
- A series of recommendations for load models for static and dynamic power system simulation studies.
- ZIP loads with larger constant power portions induce larger oscillations in transient simulations relative to ZI-E loads which are significantly more damped and converge more regularly.

Chapter Organization

The remainder of the chapter is organized as follows. Section 4.2 presents the load models we use, and section 4.3 the corresponding load portfolios. Section 4.4 discusses the test case we experiment with, section 4.5 shows results and discusses analysis, and section 4.6 concludes the paper.

4.2 Power System Loads

We define a load at the transmission level as an aggregation of all circuits and devices downstream from the transmission circuit, including but not limited to the distribution grid, commercial loads, industrial loads, domestic loads, and devices.

Power systems loads are categorized as static or dynamic. Static refers to the power consumption at that load being defined as an algebraic relationship between power and voltage. Dynamic refers to having a differential equation model for the variables that dictate power consumption. Composite loads combine both static and dynamic load models in parallel.

What is an exponential load model?

An exponential load model, also called a voltage dependent load model, relates the power consumption of the load to the normalized voltage raised to an exponent. It takes the following form.

$$P_{exp} = P_0 \left(\frac{V}{V_0} \right)^{n_P} \tag{4.1}$$

$$Q_{exp} = Q_0 \left(\frac{V}{V_0} \right)^{n_Q} \tag{4.2}$$

Here, P_0, Q_0, V_0 are the nominal real power, reactive power, and voltage magnitude for the load. V is the voltage magnitude at the load. n_P and n_Q are the exponents of the model.

The exponential model is inherently a static load model because the voltage magnitude V which dictates the power consumed by the load is determined by the network, and does not vary as a function of the load behavior.

What is a constant impedance load model?

A constant impedance load model is an exponential load model with $n_P = n_Q = 2$. It is a load that has a fixed resistance and reactance at a steady state operating frequency.

$$P_Z = P_0 \left(\frac{V}{V_0}\right)^2 = \frac{P_0}{V_0^2} V^2 = \frac{1}{R_0} V^2 \tag{4.3}$$

$$Q_Z = Q_0 \left(\frac{V}{V_0}\right)^2 = \frac{Q_0}{V_0^2} V^2 = \frac{1}{X_0} V^2 \tag{4.4}$$

Here R_0 is the constant resistance, which is independent of frequency, and X_0 is the constant reactance which is a function of the equivalent circuit's inductance and capacitance, and the frequency of the signal applied across it.

Therefore, this model has an electrical representation of a resistor in parallel with an inductor.

What is a constant current load model?

A constant current load model is also a subclass of an exponential load model with $n_P = n_Q = 1$. It is a load whose current phasor is constant over time.

$$P_I = P_0 \left(\frac{V}{V_0}\right)^1 = \frac{P_0}{V_0} V = I_{0,r} V \tag{4.5}$$

$$Q_I = Q_0 \left(\frac{V}{V_0}\right)^1 = \frac{Q_0}{V_0} V = I_{0,i} V \tag{4.6}$$

Here, $I_{0,r}$ and $I_{0,i}$ are the real and imaginary currents drawn by the load. So this model has an electrical representation of two parallel-connected constant current sources, one consuming real power at a voltage V and real current $I_{0,r}$ and another consuming reactive power at the same voltage V and imaginary current $I_{0,i}$. The overall magnitude of this current can be computed by $I_0 = ||\boldsymbol{I_0}||_2 = \sqrt{I_{0,r}^2 + I_{0,i}^2}$, where $\boldsymbol{I_0}$ is the load's current phasor.

What is a constant power load model?

A constant power load model is an exponential load with $n_P = n_Q = 0$. It is a load whose real power and reactive power consumptions are constant over time.

$$P_P = P_0 \left(\frac{V}{V_0}\right)^0 = P_0 \tag{4.7}$$

$$Q_P = Q_0 \left(\frac{V}{V_0}\right)^0 = Q_0 \tag{4.8}$$

This model has an electrical representation of two parallel connected constant power sources, one consuming real power P_0 and another consuming reactive power Q_0 at the same voltage V. For a given change in voltage, the load adjusts its current consumption to keep delivering constant power.

What is a ZIP load?

A ZIP or polynomial load is the convex combination of three exponential loads: a constant impedance load model, a constant current load model, and a constant power load model. Mathematically it is defined as follows.

$$P_{ZIP} = P_0 \left(\eta_Z \left(\frac{V}{V_0} \right)^2 + \eta_I \frac{V}{V_0} + \eta_P \right) \tag{4.9}$$

$$Q_{ZIP} = Q_0 \left(\gamma_Z \left(\frac{V}{V_0} \right)^2 + \gamma_I \frac{V}{V_0} + \gamma_P \right) \tag{4.10}$$

η_Z, η_I, η_P and $\gamma_Z, \gamma_I, \gamma_P$ are weights for each load type. Electrically, it is equivalent to the three loads in parallel.

Remark. *In the this discussion, the power consumed by a load is determined by the voltage magnitude, V, at the bus which it's connected.*

For a quasi-static phasor (QSP) simulation that does not model TL dynamics, this voltage comes from the forward propagation of a power flow solution.

For an EMT balanced dq simulation as we will perform in this study, this voltage will come from the TL's capacitor's voltage state. Said capacitor will have v_d and v_q components and so $V = ||\boldsymbol{v}_{dq}||_2 = \sqrt{v_d^2 + v_q^2}$.

What is a power electronic load model?

In this study, we model E loads as GFL inverters with standard real and reactive power outer loop PI controls, PI inner loop current controls, an averaged inverter model, a phase-locked loop, and an LCL filter, as in [24].

Contrary to the ZIP load, an E load is a dynamic load model because the current drawn is described by a differential equation. The power consumed by an E load model is:

$$P_E = \frac{1}{2}(v_d i_d + v_q i_q) \tag{4.11}$$

$$Q_E = \frac{1}{2}(v_q i_d - v_d i_q) \tag{4.12}$$

v_d, v_q are the load bus' per unit capacitor voltage dq components. i_d and i_q are the per unit current dq components drawn by the inverter defined by a system of ordinary differential equations. A detailed modeled can be found in [25].

What is a ZIP-E load model?

A ZIP-E load is a convex combination of a ZIP load and an E load model, and the power it consumes is as follows.

$$P_{ZIP-E} = P_{ZIP} + P_E = P_0 \left(\boldsymbol{\eta}^\top \boldsymbol{L_P}\right) \tag{4.13}$$
$$Q_{ZIP-E} = Q_{ZIP} + Q_E = Q_0 \left(\boldsymbol{\gamma}^\top \boldsymbol{L_Q}\right) \tag{4.14}$$

where

$$\boldsymbol{\eta} = \begin{bmatrix}\eta_Z & \eta_I & \eta_P & \eta_E\end{bmatrix}^\top \tag{4.15}$$
$$\boldsymbol{\gamma} = \begin{bmatrix}\gamma_Z & \gamma_I & \gamma_P & \gamma_E\end{bmatrix}^\top \tag{4.16}$$

and

$$\boldsymbol{L_P} = \begin{bmatrix}\left(\frac{V}{V_0}\right)^2 & \left(\frac{V}{V_0}\right)^1 & \left(\frac{V}{V_0}\right)^0 & \frac{1}{2}(v_d i_d + v_q i_q)\end{bmatrix}^\top \tag{4.17}$$
$$\boldsymbol{L_Q} = \begin{bmatrix}\left(\frac{V}{V_0}\right)^2 & \left(\frac{V}{V_0}\right)^1 & \left(\frac{V}{V_0}\right)^0 & \frac{1}{2}(v_q i_d - v_d i_q)\end{bmatrix}^\top \tag{4.18}$$

Note the addition of the η_E and γ_E terms which capture the power consumed by the E part of the load. Moreover, it is now the case that the load consumes real and reactive power not only as a function of the voltage at the load bus, but also as a function of the current drawn by the load. [1]

4.3 Load composition

Based on a study of the literature, there is no standardized way to choose ZIP load coefficients based on an understanding of the load behavior. Therefore, we outline modeling options based on what industry has done, and propose alternatives.

One option is as it was done in the 1980s [11]: real power loads as static constant current loads, and reactive power loads as static constant impedance loads. Another is what was done in the 2000s: real and reactive power loads as static ZIP loads, as in (4.9) and (4.10). However, it's not clear how to select coefficients [54]. Based on [54], the USA is the only country where a substantial number of industry members run simulations with composite load models. [51] proposes a few coefficient options for the last two options.

New scenarios and benchmarks

We consider a constant impedance test case as a benchmark, as this is the most common load type in research. We consider cases with P or E load contributions (through η_P and η_E, respectively) in 10 percentage point increments from 0 to 100% with the remainder of the

[1] We develop `ZIP-E_loads.jl`, an open source Julia-based package to extend the modeling capabilities of `PowerSimulationsDynamics.jl (PSID.jl)`. It leverages already available models in `PSID.jl` to allow the user to model ZIP-E load variations.

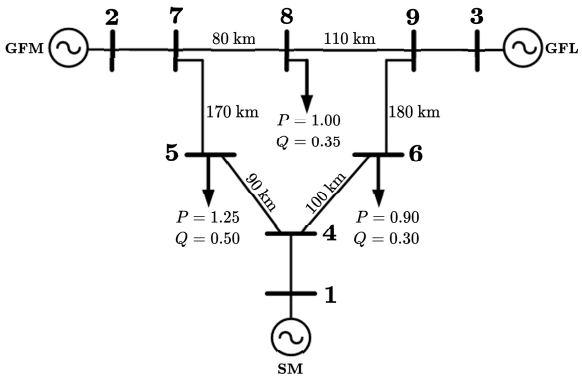

Figure 4.1: Modified IEEE 9 bus test system. SM at bus 1 (reference bus), VSM GFM at bus 2, GFL at bus 3. Note that we do not use a slack bus for our simulations.

load constituting of equal parts Z and I, thus comparing ZIP loads to ZI-E loads by choosing $\boldsymbol{\eta}, \boldsymbol{\gamma}$ as follows.

$$\boldsymbol{\eta} = \boldsymbol{\gamma} = \begin{bmatrix} \frac{1-x}{2} \\ \frac{1-x}{2} \\ x \\ 0 \end{bmatrix}, \begin{bmatrix} \frac{1-x}{2} \\ \frac{1-x}{2} \\ 0 \\ x \end{bmatrix} \quad \forall x \in \{0, 0.1, \ldots, 1.0\}$$

Note that for each x we have a particular load portfolio. Constant power and full E loads are defined by $x = 1.0$. This comparison will allow us to test differences of the effects modeling power electronic loads as P loads or E loads.

4.4 Test Case

In this work, we use the IEEE WSCC 9 Bus test case shown in Fig. 4.1. It is composed of a synchronous machine (SM), a grid-forming converter (GFM) operating as a virtual-synchronous machine (VSM), and a GFL inverter as sources. It has three loads, and six transmission lines. For lines, we use algebraic and dynamic π line models, *statpi* and *dynpi* respectively. Models and data for these devices are according to [10, 38]. We stay consistent in our choice of model for purposes of comparing results across papers.

Experiments

The network's nominal operating condition is found by solving a power flow, and then loads are scaled by a constant factor we denote *load scale*. We then scale all generator power set points in proportion to *load scale*. For each load model, for each line model, and for each *load scale* value, we run a small signal and transient analysis.

For the small signal studies, given a single *load scale* value (or, equivalently, a network loading condition), all line and load models will produce the same power flow solution. We verify the stability of this operating condition to address our guiding questions.

For the transient analysis, we trip the second heaviest loaded branch as given by the power flow solution, which is the line connecting buses 4 and 5 in this case. We choose to measure the current flowing into the network at Bus 3 as a proxy variable for inverters since it could be saturated if control limits are reached. We evaluate time domain simulations to see current behavior difference to address our guiding questions.

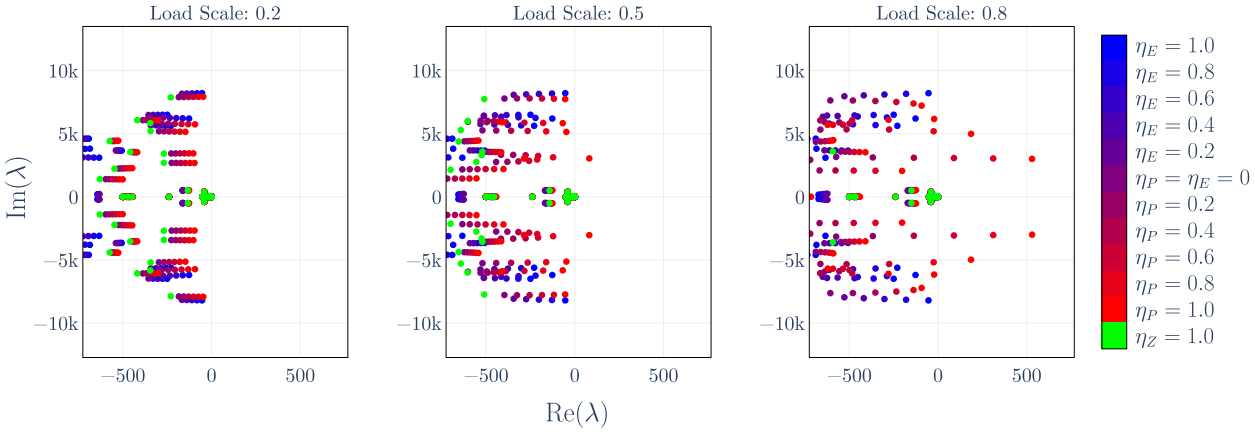

Figure 4.2: Network eigenvalues with *dynpi* line model at *load scales* of 0.2, 0.5, and 0.8 increasing to the right.

4.5 Simulation Results and Analysis

Code and results are publicly available in our GitHub repository for reproduction, which includes a set of interactive plots for the reader to further explore our results if interested.

Small Signal Analysis

Load model effect

When comparing eigenvalues of ZI-E loads with high E values to ZI-E loads with low E values, there was no consistent trend. Some shifted to the right, others to the left, this is likely dependent on the influence of particular states on those eigenvalues. This is also true for ZIP loads. This can be appreciated in Fig. 4.2.

Results further showed that at low network loading levels, load model variations had limited effect on eigenvalues and thus on stability conclusions. This can be seen in the leftmost plot in Fig. 4.2, with all load models concluding in a stable operating condition.

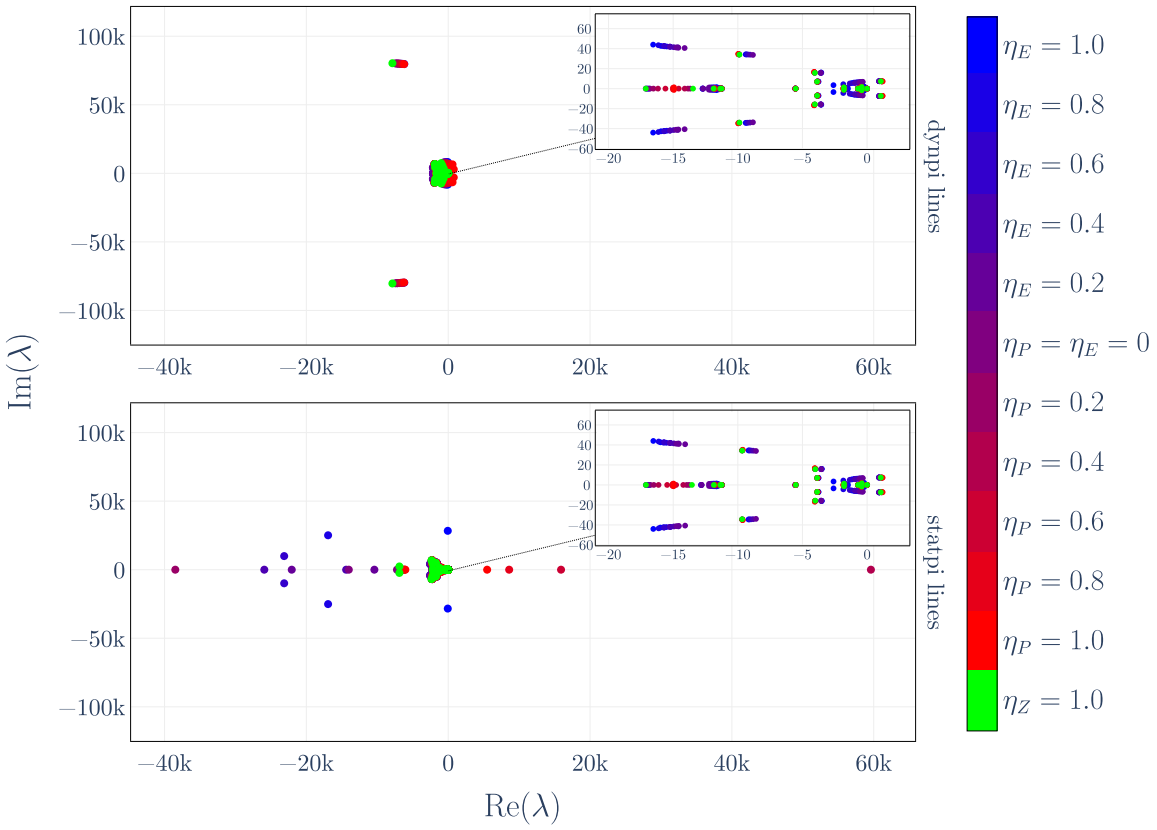

Figure 4.3: Eigenvalues at *load scale* = 1.0 for *dynpi* (top) and *statpi* (bottom) line models. ZI-E loads are in blue and ZIP loads are red in 10% increments as given by the heatmap bar on the right.

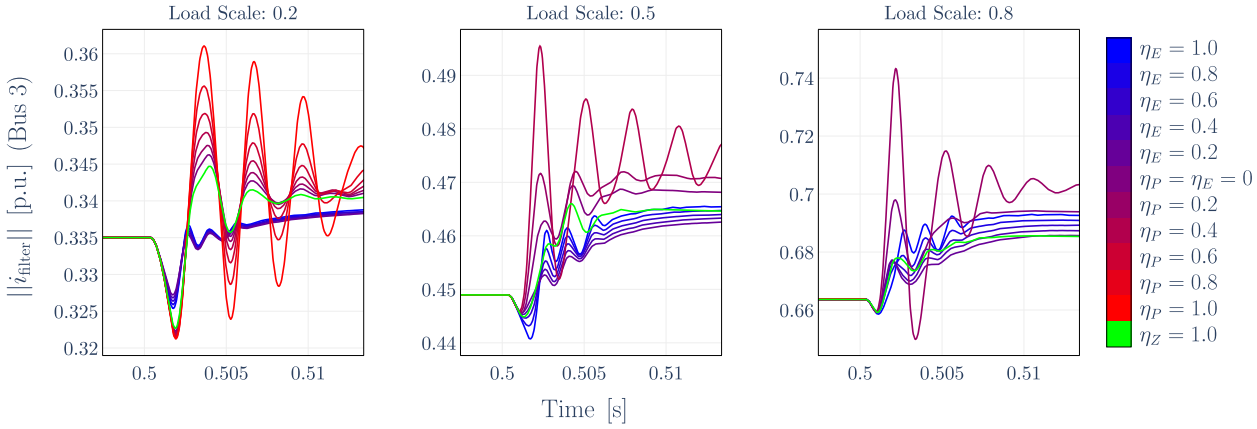

Figure 4.4: Bus 3 inverter current magnitude after a branch trip on line 4-5 with *dynpi* lines.

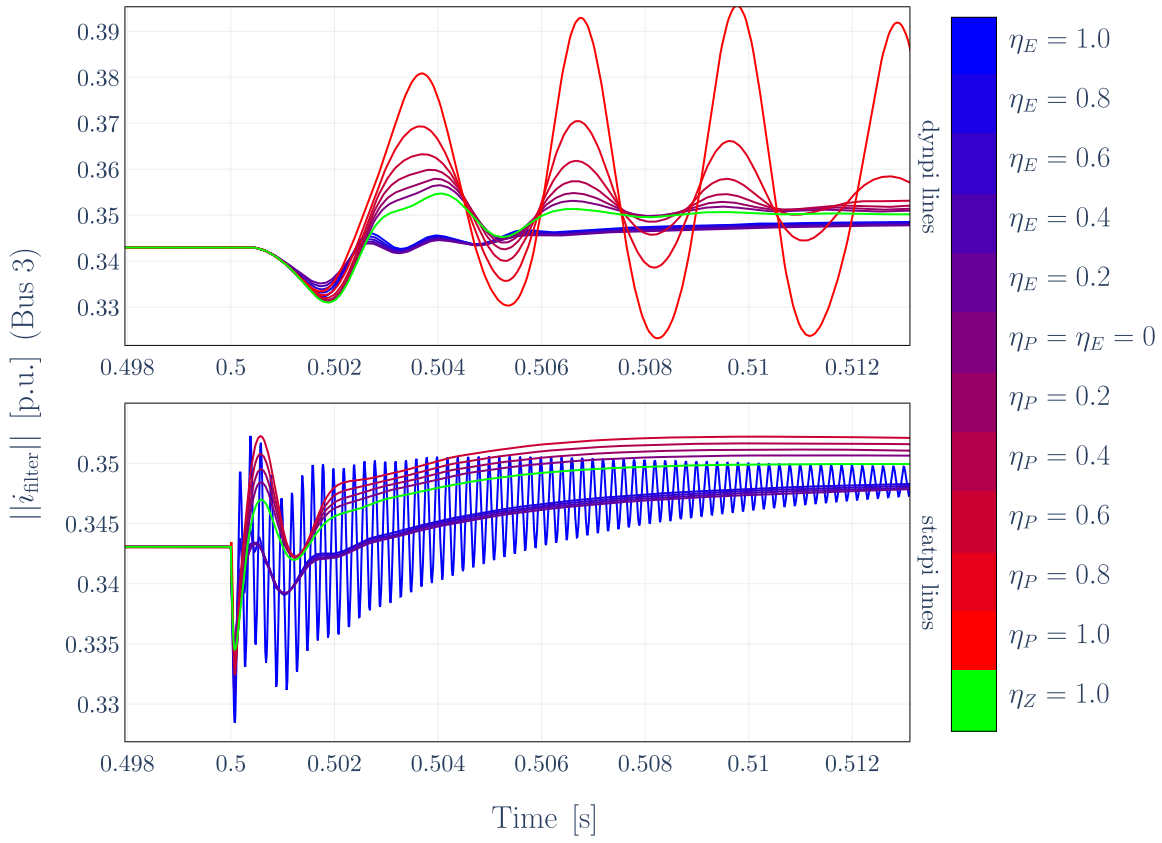

Figure 4.5: Transient simulation of Bus 3 inverter current magnitude after a branch trip of line connecting Bus 4 and Bus 5. *load scale* = 0.25.

This suggests that when the network has enough buffer between the operating condition and the instability boundary, the choice of load model has a small impact on system behavior and stability conclusions.

As we increase the network loading, however, we find that ZIP load cases move the eigenvalues to the right more quickly than ZI-E loads. Several cases showed a stable operating conclusion with ZI-E loads, but an unstable conclusion with ZIP loads. The center plot in Fig. 4.2 shows an example.

As the network loading further increased, we found that the eigenvalues for ZIP load cases were very far right on the complex plane, whereas eigenvalues for ZI-E cases were unstable but very close to the $j\omega$ axis with real parts less than 1. This suggests that, despite being an unstable operating condition, it is much more stable relative to the common industry practice of ZIP loads. This can be appreciated on the rightmost plot of Fig. 4.2. Further, because these ZI-E cases are barely unstable, this operating condition might be stable with differently tuned controller gains for the generating devices.

Lastly, in addition to eigenvalues moving to the right under higher loading, the effect

of load model on a particular eigenvalue is more pronounced as evidenced by more spread eigenvalue maps on Fig. 4.2 as loading increases.

These results support the hypothesis that a low stability margin correlates with higher sensitivity to load model choice presented in [29]. In situations where the distance to the instability boundary is small, modeling constant power loads with the typical algebraic model could lead to significantly overestimated instability. The E component seems to aid in remedying this.

Load model effect with line dynamics assumption

A consistent theme across all cases was the stabilizing effect of the *dynpi* line model, particularly at higher load scales. An example of this can be seen in Fig. 4.3 where eigenvalues for the *stapi* model have significantly larger real parts relative to *dynpi* model. For the *statpi* model we found several cases in which there is a singularity where an eigenvalue moves from minus infinity to positive infinity as loading is increased, suggesting a modeling limitation. This does not happen for the *dynpi* model. Further, *dynpi* lines tended to filter out many high frequency eigenvalues with the exception of complex conjugate pairs with frequency of about 12.5 kHz suggesting they could be high frequency states of the dynamic lines, these are the cluster on the top plot of Fig. 4.3. All other eigenvalues had frequencies less than 1.2 kHz, whereas for the *statpi* case, many unfiltered modes had frequencies of about 4-5 kHz. Further, we had several line parameters and changing between them didn't significantly affect the placement of the least stable eigenvalues nor the dynamic behavior of the variables we considered.

Transient analysis

For the transient analysis, we measure the magnitude of the GFL inverter's filter current at Bus 3.

Load model effect

We typically saw two families of traces post disturbance: one trace family for ZIP loads and another for ZI-E loads. When they both converged, they had the same steady-state solution but different ways to reach it. Cases with ZIP loads had larger overshoots relative to cases with ZI-E loads. Further, ZIP cases with larger P percentages tended to have larger amplitude than those with lower P percentages. The same was true for ZI-E cases. This can be appreciated in the leftmost plot of Fig. 4.4.

Further, as *load scale* increased, cases with higher ZIP were the first to destabilize, which is consistent with the small signal analysis. This is further appreciated in the center and rightmost plots in Fig. 4.4 where several of the high-P cases fail to converge, and those that do converge have significantly larger overshoots relative to all the ZI-E cases. This implies

that E loads induced more damping relative to P loads for both low and high-frequency oscillations.

The long-term oscillations of the ZI-E loads were not ultimately problematic. In stable cases, they disappear quickly, and in unstable cases, they follow a similar trend to ZIP loads.

Load model effect with line dynamics assumption

High-frequency oscillations on *statpi* lines were seen for both high-E and high-P loads, but decreased rapidly with decreasing E or P percentage. Only high-E loads show these oscillations because in high P cases they grew too large and the simulations did not converge.

In most cases, the *dynpi* line model clearly filters thr 4-5 kHz frequency modes in the system present in the *statpi* case. This is consistent with the small signal analysis, and can be appreciated in Fig. 4.5.

Network loading

Under this SM-GFM-GFL generation configuration, the network loading needed to be low ($load\ scale = 0.2$) to ensure a stable operating condition for all load and line models. We compared this to the case with SMs in all generation buses and found that for $load\ scale = 1.0$ the network equilibrium was stable except for ZIP loads with $\eta_P > 0.4$ with both *stapi* and *dynpi* lines. This complements the finding that ZIP loads are the most difficult loads to stabilize, and speaks to the relevance of generation configuration contributing to the stability of the equilibrium condition.

Computational burden

Networks with ZI-E loads have about 30 more dynamic states than those with ZIP loads due to the three E loads. Despite that, we found that *statpi* cases' runtime was not significantly impacted, and *dynpi* simulations with ZI-E loads ran $7 - 10\times$ faster than corresponding ZIP load cases, suggesting that ZIP loads can be more computationally intensive than corresponding ZI-E loads.

4.6 Conclusions

In this work we perform small signal and transient stability analyses for power systems using a new composite load model, ZIP-E loads, for more realistic power electronics load modeling of power systems at the transmission level. We further develop `ZIPE_loads.jl`, an open-source load modeling package to model these loads in `PSID.jl`. We perform experiments on the IEEE WSCC 9 Bus test case to test how changing line and load models affect stability.

In the context of our guiding questions, we found that: i.) The choice of load model matters less when the network is lightly loaded, which corresponds to when the operating

condition is far from its stability boundary. As the system is more heavily loaded and approaches the stability boundary, eigenvalue placement changes more drastically in relation to the load model, and ZIP loads result in an unstable operating condition significantly earlier than corresponding ZI-E loads. ii.) ZI-E loads showed a different family of traces relative to ZIP loads: they showed more damping, significantly smaller overshoots, and convergence to the slow modes much quicker. While overall trajectories of ZI-E loads are different than ZIP loads, they have the same steady state behavior in cases where both converge, as expected.

We conclude that in general load models are important for both small signal and transient analysis for power system, especially under stressed conditions. Approximating power electronics loads behavior as ZIP loads could result in unrealistic unstable conclusions far more quickly than could actually happen. The conclusions drawn from cases with ZI-E loads can be significantly different from those with ZIP loads both for small signal and transient analysis. Because of the large amounts of power electronic loads getting connected on the network, we believe ZIP-E loads make a promising attempt and capturing their dynamics so that we can arrive at reliable and trustworthy results.

This work results in the following recommendations: i.) if a particular system is operating at a condition far from a stability boundary, and that is known prior to running a simulation, pick the least expensive computational load or easility to interpret model, a constant impedance model would be suitable, ii.) if the network is close to a stability boundary, constant power loads will overestimate instability, therefore, use ZI-E load models, iii.) between *statpi* and *dynpi* line models, use *dynpi* for both transient and small signal analyses.

Future work includes changing the location of the generators, the generation portfolio, and varying the system's grid strength to explore low-frequency oscillations.

Chapter 5

Analysis of relationships between abc and dq reference frame signals

Previous chapters have looked at modeling specific components at the generation, transmission and load level for power system analysis. In this chapter, we take a general modeling framework applicable to all levels of power system modeling to understand the relationships between signals with frequencies across different coordinate or reference frames. Specifically, we derive precise relationships between signals in *abc* and *dq* coordinate frames for modeling and producing specific conclusions for power systems.

Introduction

Power systems are modeled relative to a specific choice of coordinate frame. This influences the mathematical model that describes its physical behavior. Depending on the application, a particular choice of reference frame may be desired over another in order to facilitate the analysis.

The static *abc* reference frame is the first introduced in power systems engineering because it represents its physical behavior. Other reference frames include the $\alpha\beta 0$ frame, another static reference frame, and the rotating $dq0$ reference frame. Modeling with respect to these reference frames is done by projecting a space phasor onto the *abc*, $\alpha\beta 0$, and $dq0$ frames [67]. A signal modeled in one of these reference frames can be converted to another via transformations. In the specific case of balanced three phase *abc* signals, which we will focus on in this chapter, the 0-component of either the $\alpha\beta 0$ or $dq0$ representation is zero for all time. We therefore drop this component and refer to $\alpha\beta$ and dq coordinate frames.

A three phase *balanced abc* signal is characterized by an amplitude and phase angle because the phase shifts are predefined to be $\frac{2\pi}{3}$ between each pair of phases, and the frequencies of all signals are the same. Thus three signals are a redundant description of the behavior. All the information in the three *abc* signals can be captured by two signals in the static $\alpha\beta$ frame. Note that because the *abc* and $\alpha\beta$ reference frames are static, a space phasor projected onto either frame will produce signals of the same frequencies.

A *dq* reference frame rotates at a particular frequency. System representations in this coordinate frame are useful for power system analysis because signals that oscillate in the *abc* frame at the *dq* reference frequency will converge to constant values in the *dq* state space. This makes analysis and control more straightforward in the *dq* frame.

Transmission system operators (TSOs) are interested in oscillations in the *abc* frame since this is what is physically measured, yet it is often convenient to perform power system analysis in a *dq* reference frame. Therefore, a precise understanding of how oscillations in the *dq* frame project onto the *abc* frame and vice-versa is necessary. While transformations between the reference frames are well understood, some information is hard to keep track of during the transformation process. Given a time domain *abc* signal, it is straightforward to apply a transformation and project it onto the *dq* frame, however, the corresponding frequencies in the *dq* frame are not obvious.

While ideas to map frequencies in the *dq* frame to *abc* have been discussed in the literature, a precise mapping between them has yet to emerge. For example, [57] and [48] present geometric interpretations of the translation of signals across frames. While providing useful intuition on the geometry of the transformations, they do not provide a mathematical relationship between the frequencies of signals *abc* and $\alpha\beta$ frames to the *dq* frame, nor vice-versa. In [66], the authors state that the relationship between *dq* and $\alpha\beta$ signals is dependent on the control structure and further claim that "it is not straightforward to predict the actual oscillations in the $\alpha\beta$-frame based on the modal analysis results in the *dq*-frame". In [65], the authors claim – without rigorous support – that a difference in symmetry (different dynamics on the d versus q axis) results in specific oscillations in the $\alpha\beta$ frame. The current chapter takes a signals-based approach to address this gap in knowledge about transforming *dq* signals to $\alpha\beta$ or *abc*.

5.1 The space phasor and its projections

The space phasor is an abstract quantity that is projected onto the different coordinate frames to generate signals in different frames. Consider an *abc* three-phase balanced signal as follows:

$$x_a(t) = \hat{x}\cos(\omega t + \theta_0), \quad x_b(t) = \hat{x}\cos(\omega t + \theta_0 - 2\pi/3), \quad x_c(t) = \hat{x}\cos(\omega t + \theta_0 - 4\pi/3)$$

with identical magnitudes $\hat{x}$, identical frequencies $\omega = 2\pi f$, and phase angle θ_0 with phase shifts of $\frac{2\pi}{3}$ between all phases. Note that $x_a(t), x_b(t), x_c(t)$ are one-dimensional continuous functions.

A space phasor is defined by

$$\vec{x}(t) \equiv \frac{2}{3}(x_a(t)e^{j0} + x_b(t)e^{j2\pi/3} + x_c(t)e^{j4\pi/3}) \tag{5.1}$$

where $e^{jz} = \cos(z) + j\sin(z)$, with $j = \sqrt{-1}$, is a rotation of a signal by z radians. Note that $\vec{x}(t) = \hat{x}e^{j(\omega t+\theta_0)} = \sqrt{2}\underline{\mathrm{x}}e^{j\omega t}$, where $\underline{\mathrm{x}} = \frac{1}{\sqrt{2}}\hat{x}e^{j\theta_0}$ is the traditional definition of the RMS

static phasor when we have the three phase balanced signals above. Given a space phasor, we will be projecting onto the *abc*, the $\alpha\beta$, the *dq* coordinate frames.

abc **frame**

Given a space phasor $\vec{x}(t)$, the *abc* components are:

$$x_a(t) = \mathbf{Re}\{\vec{x}(t)\}, \quad x_b(t) = \mathbf{Re}\{e^{-j\frac{2\pi}{3}}\vec{x}(t)\}, \quad x_c(t) = \mathbf{Re}\{e^{-j\frac{4\pi}{3}}\vec{x}(t)\}$$

$\alpha\beta$ **frame**

The α and β components are defined as

$$x_\alpha(t) = \mathbf{Re}\{\vec{x}(t)\}, \quad x_\beta(t) = \mathbf{Im}\{\vec{x}(t)\}$$

i.e. $\vec{x}(t) = x_\alpha(t) + jx_\beta(t)$.

dq frame

dq components are related to the space phasor as follows:

$$x_d(t) = \mathbf{Re}\{\vec{x}(t)e^{-j\epsilon(t)}(t)\} \quad x_q(t) = \mathbf{Im}\{\vec{x}(t)e^{-j\epsilon(t)}(t)\}$$

Here, $\epsilon(t) = \epsilon_0 + \int_0^t \omega(\tau)d\tau$, where ϵ_0 is a constant phase angle offset, and $\omega(t)$ is the frequency of the rotating frame. For constant $\omega(t) = \omega_0$, $\epsilon(t) = \epsilon_0 + \omega_0 t$. If $\omega_0 = \omega$ (the frequency of frame rotation is the space phasor's frequency), then

$$x_d(t) + jx_q(t) = \hat{x}\cos(\theta_0 - \epsilon_0) + j\hat{x}\sin(\theta_0 - \epsilon_0)$$

Since θ_0 and ϵ_0 are constant, $\cos(\theta_0 - \epsilon_0)$ and $\sin(\theta_0 - \epsilon_0)$ are as well. Therefore if the reference frame rotates at the signal's frequency, then time-varying signals in the *abc* and $\alpha\beta$ frames project to static quantities on the *dq* frame.

Note that the notation in this section uses the subscript of the x variables to refer to the reference frame relative to which this variable is measured. Due to indexing, reference frames, and different variables all being degrees of freedom that we need to choose, we slightly abuse notation throughtout this work while making it clear what subscripts mean in each case.

5.2 *abc* signals to *dq* signals

A single phase time domain evolution can be represented as the superposition of N signals with constant different amplitudes $\hat{x}_i$, frequencies $\omega_i = 2\pi f_i$, and phase shifts θ_i, as follows: $x_a(t) = \sum_{i=1}^N \hat{x}_i \cos(\omega_i t + \theta_i)$, $x_b(t) = \sum_{i=1}^N \hat{x}_i \cos(\omega_i t + \theta_i - 2\pi/3)$, $x_c(t) = \sum_{i=1}^N \hat{x}_i \cos(\omega_i t +$

$\theta_i - 4\pi/3$). Each three pair of signals will have its own space phasor, all of which superpose into a composite space phasor:

$$\vec{x}(t) = \sum_{i=1}^{N} \hat{x}_i e^{j\theta_i} e^{j\omega_i t}. \tag{5.2}$$

We can project this onto the coordinate frames of interest to inspect how signals manifest. Note that in general $\hat{x}_i$ can be a function of time, $\hat{x}_i(t)$.

Projection onto the $\alpha\beta$ frame

The $\alpha\beta$ components are

$$x_\alpha(t) = \sum_{i=1}^{N} \hat{x}_i \cos(\omega_i t + \theta_i) \quad x_\beta(t) = \sum_{i=1}^{N} \hat{x}_i \sin(\omega_i t + \theta_i).$$

Observations

- The amplitudes $\hat{x}_i$, frequencies $\omega_i = 2\pi f_i$, and phase shifts θ_i of the $\alpha\beta$ components are those of the *abc* components, and of each other: these quantities are preserved from *abc*.
- There is a phase offset between components from $\cos(\cdot)$ in α and $\sin(\cdot)$ in β. For $f_i > 0$, the β component *lags* the α component by $\frac{\pi}{2}$. For $f_i < 0$ β *leads* α by $\frac{\pi}{2}$.
- α and β components of arbitrarily many superimposed three phase balanced *abc* signals are also superimposed.

Projection onto the dq frame

The dq components are

$$x_d(t) = \sum_{i=1}^{N} \hat{x}_i \cos((\omega_i - \omega_0)t + \theta_i - \epsilon_0) \tag{5.3}$$

$$x_q(t) = \sum_{i=1}^{N} \hat{x}_i \sin((\omega_i - \omega_0)t + \theta_i - \epsilon_0). \tag{5.4}$$

Observations

- The $\alpha\beta$ observations in Section 5.2 also apply for dq.
- Three phase balanced *abc* signals will project with frequency $|f_i - f_0|$ on dq axes. Thus, frequencies $f_i < 2f_0$ in *abc* will manifest as less than f_0 in dq, implying that two *abc* frequencies can result in the same dq frequency.

5.3 *dq* signals to *abc* signals

In this section we consider transforming *dq* signals into *abc* signals. We take a slightly different approach here because it is common to write a *dq* representation of a system in linear state-space form. While this is also possible with an *abc* representation, due to the nonlinearity of power systems, an equilibrium point is required for the linearization process and choosing one in *abc* coordinates does not have a clear meaning because equilibria are technically limit cycles and not points. On the contrary, a nonlinear power system model in *dq* coordinates can be linearized around an equilibrium point because sinusoidal trajectories in *abc* converge to points in *dq*.

Consider linearized dynamics around an equilibrium point for a system modeled in the *dq* reference frame

$$\dot{x} = Ax$$

where $x \in \mathbf{R}^n$ is the differential state vector for the linearized system, and $A \in \mathbf{R}^n \times \mathbf{R}^n$ is the state matrix. Note that in this section x refers to the n-dimensional state vector in *dq* coordinates.

When A is diagonalizable, the time domain evolution of the states can be written as $x(t) = \sum_{i=1}^{n} e^{\lambda_i t} x(0)$ where $\lambda_i = \gamma_i + j\xi_i$ is the i^{th} eigenvalue, and $x(0) \in \mathbf{R}^n$ is the initial condition. When A is not diagonzalizable, its Jordan form can be computed and a similar process can be followed.

Further, if the eigenvectors of A are linearly independent, then they form a basis for the vector space and the initial condition $x(0)$ can be expressed as their linear combination: $x(0) = \sum_{i=1}^{n} c_i v_i$, where $v_i \in \mathbf{C}^n$ is the i^{th} eigenvector, and $c_i \in \mathbf{C}$ are the corresponding coefficients to make the initial condition a linear combination of the eigenvectors. Therefore,

$$x(t) = \sum_{i=1}^{n} c_i e^{\gamma_i t} e^{j\xi_i t} v_i \tag{5.5}$$

A particular state $x_k(t)$ of the state vector is then

$$x_k(t) = \sum_{i=1}^{n} c_i e^{\gamma_i t} e^{j\xi_i t} v_{ki} = \sum_{i=1}^{n} c_i |v_{ki}| e^{\gamma_i t} e^{j(\xi_i t + \theta_{ki})} \tag{5.6}$$

where $x_k(t)$ is the k^{th} entry of $x(t)$, and $v_{ki} \in \mathbf{C}$ is the k^{th} entry of eigenvector v_i; expressed in polar form as $|v_{ki}|e^{j\theta_{ki}}$. Note that in this section our notation corresponds to subscripts of x to refer to an entry (or row) of x, which is different than previous sections.

Without loss of generality $x_k(t)$ can be said to be the d component of any *dq* variable in $x(t)$, and $x_l(t)$ the corresponding q component. Therefore, a *dq* variable can be expressed as $x_k(t) + jx_l(t)$. Using polar form, we project the d signal on to the $\alpha\beta$ frame by $y_k(t) + jy_l(t) = (x_k(t) + jx_l(t))\, e^{j(\omega_0 t + \epsilon_0)}$, where $y_k(t), y_l(t)$ are the corresponding $\alpha\beta$ representations of the

variables. When we apply this, we arrive at

$$y_k(t) + jy_l(t) = \sum_{i=1}^{n} c_i|v_{ki}|e^{\gamma_i t}e^{j((\xi_i+\omega_0)t+\theta_{ki})} + j\sum_{i=1}^{n} c_i|v_{li}|e^{\gamma_i t}e^{j((\xi_i+\omega_0)t+\theta_{li})} \tag{5.7}$$

Recall that $\lambda_i = \gamma_i + j\xi_i$, meaning that the ξ_is are the frequencies of the dq variables. We now note that all eigenvalues that are purely real will have $\xi_i = 0,\ i \in \{1, \ldots, n\}$, and those that have $\xi_i \neq 0$ will appear in complex conjugate pairs. Therefore frequencies $\xi_i \neq 0$ will have an associated $-\xi_i$ term.

By inspecting (5.7) it can be seen that all frequencies $\xi_i + \omega_0$ will appear in the $\alpha\beta$ representation of the variables, and, therefore, in the abc representation as well. However, we explore the case in which it is possible for only some, not all, of the frequencies to show up.

Let us consider the case of a pair of complex conjugate eigenvalues

$$\begin{aligned}\lambda_1 &= \gamma_1 + j\xi_1\\ \lambda_2 &= \gamma_2 + j\xi_2 = \lambda_1^* = \gamma_1 - j\xi_1.\end{aligned}$$

Note that the corresponding eigenvectors will be complex conjugates of each other, $v_2 = v_1^*$, resulting in its entries $|v_{k2}|e^{j\theta_{k2}} = |v_{k1}|e^{-j\theta_{k1}},\ \forall k \in \{1, \ldots, n\}$. Further, using $j = e^{j\frac{\pi}{2}}$, we can rewrite the $\alpha\beta$ variables in (5.7) as follows.

$$\begin{aligned}y_k(t) + jy_l(t) = {} & c_1|v_{k1}|e^{\gamma_1 t}e^{j((\xi_1+\omega_0)t+\theta_{k1})} + c_2|v_{k1}|e^{\gamma_1 t}e^{j((-\xi_1+\omega_0)t-\theta_{k1})}\\ & + c_1|v_{l1}|e^{\gamma_1 t}e^{j((\xi_1+\omega_0)t+\theta_{l1}+\frac{\pi}{2})} + c_2|v_{l1}|e^{\gamma_1 t}e^{j((-\xi_1+\omega_0)t-\theta_{l1}+\frac{\pi}{2})}\\ & + \sum_{i=3}^{n} c_i|v_{ki}|e^{\gamma_i t}e^{j((\xi_i+\omega_0)t+\theta_{ki})} + \sum_{i=3}^{n} c_i|v_{li}|e^{\gamma_i t}e^{j((\xi_i+\omega_0)t+\theta_{li}+\frac{\pi}{2})}\end{aligned}$$

We now focus our analysis on the first four terms which will contain the information on a pair of complex conjugate eigenvalues. We note that if, for example, the $-\xi_1$ terms sum to zero, this frequency will not appear in the $\alpha\beta$ frame. This is captured in the following equality constraint.

$$c_2 e^{\gamma_1 t}e^{j((-\xi_1+\omega_0)t)}\left(|v_{k1}|e^{-j\theta_{k1}} + |v_{l1}|e^{-j(\theta_{l1}-\frac{\pi}{2})}\right) = 0,\ \forall t \tag{5.8}$$

From inspection it is clear that $c_2 e^{\gamma_1 t}e^{j((-\xi_1+\omega_0)t)} \neq 0$ because the c_i's are the coefficients to represent the initial condition as a function of the eigenvectors. So, for this condition to hold the term within parethesis must be zero, for which it is necessary that $|v_{k1}| = |v_{l1}|$, which reduces the condition to

$$\left(e^{-j\theta_{k1}} + e^{-j(\theta_{l1}-\frac{\pi}{2})}\right) = 0,\ \forall t.$$

Using $-1 = e^{j\pi}$, this reduces to $e^{-j\theta_{k1}} = -e^{-j(\theta_{l1}-\frac{\pi}{2})} = e^{-j(\theta_{l1}-\frac{\pi}{2}-\pi)}$. This implies that $-\theta_{k1} = -\theta_{l1} + \frac{3\pi}{2}$.

Therefore, we have established that (5.8) holds when both $|v_{k1}| = |v_{l1}|$ *and* $\theta_{l1} = \theta_{k1} + \frac{3\pi}{2}$. This implies that the eigenvector v_1 has two entries, k, l, that share the same magnitude and share a specific phase relationship, namely one leads the other by $\frac{3\pi}{2}$. So, for this to be true, two conditions need to simultaneously hold: the magnitude condition, and the phase condition.

A similar condition is obtained when setting the terms with $+\xi_1$ to zero. In this case, $|v_{k2}| = |v_{l2}|$ and $\theta_{l2} = \theta_{k2} + \frac{3\pi}{2}$. This means that the relevant information for this case is associated to eigenvector v_2.

It is worth noting that if $|v_{k1}| = |v_{l1}|$, then it will also be true that $|v_{k2}| = |v_{l2}|$ because $v_2 = v_1^*$. It can also be proven that only one of the angle conditions can be true at once. Therefore, which of the angle conditions is satisfied will determine which frequency, ξ_1 or $-\xi_1$, persists in $\alpha\beta$ coordinates. If both conditions are not satisfied at once, then both frequencies will appear.

This analysis can be extrapolated to any n and can be analyzed on an individual state (other indexes different from k, l) or eigenvalue (different indexes from $1, 2$) basis. This will uniquely be able to inform how dq frequencies ξ_i will show up in $\alpha\beta$.

To summarize, for a non-zero dq eigenvalue frequency, there are three possibilities as to how it may appear in the $\alpha\beta$ and abc reference frames. Knowing that they will appear in complex conjugate pairs, and without loss of generality saying that $\xi_2 = -\xi_1$, the results are:

- For a pair of dq states with indexes k, l only a frequency of $\xi_1 + \omega_0$ will appear if both $|v_{k2}| = |v_{l2}|$ and $\theta_{l2} = \theta_{k2} + \frac{3\pi}{2}$ hold.
- For a pair of dq states with indexes k, l only a frequency of $-\xi_1 + \omega_0$ will appear if both $|v_{k1}| = |v_{l1}|$ and $\theta_{l1} = \theta_{k1} + \frac{3\pi}{2}$ hold.
- For a pair of dq states with indexes k, l both $\xi_1 + \omega_0$ and $-\xi_1 + \omega_0$ frequencies will appear if any of the two conditions (magnitude or angle) do not hold.

Observations

- Constants in dq ($\xi_i = 0$) have frequency $\omega_0 = 2\pi f_0$ in abc.
- In general, frequencies $\xi_i = 2\pi f_i$ in dq will show up as two signals in abc: one of frequency $|f_0 + f_i|$ and another with frequency $|f_0 - f_i|$.
- Note that if $f_0 - f_i < 0$, the signal will still have frequency of $|f_0 - f_i|$. The negative will imply that there is a π phase shift on the signal.
- When specific angle and phase conditions are met, only one of the two possible $|f_0 + f_i|$ and $|f_0 - f_i|$ frequencies will appear in abc.

These results are in alignment with those found from projecting three phase *abc* balanced signals onto the *dq* frame.

Amplitude modulation in *abc* from sub- and supersynchronous modes

When $f_i < 2f_0$, *abc* signals will generally have oscillations at both sub- and supersynchronous frequencies (i.e., when one of magnitude and phase conditions is not satisfied), and those frequencies will be equally far from f_0: $||(f_0 + f_i)| - f_0)| = ||(f_0 - f_i)| - f_0|$. This implies that

$$\cos(2\pi(f_0 + f_i)t) + \cos(2\pi(f_0 - f_i)t) = 2\cos(2\pi f_i t)\cos(2\pi f_0 t)$$

which corresponds to amplitude modulation of a signal at frequency at which the *dq* frame rotates, f_0, by another of frequency of the *dq* signals f_i.

5.4 Conclusions

In this chapter we present a detailed analysis on how to precisely predict how a *dq* analysis can be used to make conclusions about *abc* quantities. While these conditions are sufficient for the conclusions presented, further study is required to determine if they are also necessary conditions.

Chapter 6

Summary and conclusions

In this thesis I have presented an electrical engineering approach to address the modern societal challenge of climate change in the 21st century, and the changes occurring in modern power systems due to the use of new technologies. Using mathematical modeling methods, I present conclusions and recommendations that enhance our understanding of modern power systems.

Chapter 1 introduces the societal problem of climate change, its impact on human quality of life, and recent trends suggesting that renewable energy resource adoption will continue to increase. Along with this increase, electrical power systems are seeing rise a series of engineering challenges which are also introduced and are present in all levels of power systems: generation, transmission, and consumption of electricity.

Chapter 2 tackles this challenge at the generation level. It presents the first known provably safe hybrid control for sinusoidal reference tracking of the half-bridge inverter that is able to consider a changing reference signal coming from a grid-forming control strategy.

Chapter 3 takes another vantage point and tackles this challenge at the transmission level. It shows the results of detailed small signal and dynamic simulation studies to determine what level of transmission line modeling fidelity is required for modern power system analysis to achieve conclusions that are accurate in modern power systems. It concludes that a dynamic π transmission line model is a suitable model choice for accurate results in small signal and dynamic simulation analysis of power systems.

Chapter 4 also looks this challenge from the load perspective. It presents a newly proposed ZIP-E load model able to capture the industry standard ZIP load, alongside a dynamic power electronic inverter model. We perform small signal and dynamic simulation analysis to see how changing load profiles to reflect modern loads affects stability conclusions, and find that power electronic loads actually enhance grid stability.

Lastly, Chapter 5 provides a precise theoretical result allowing us to perform dq power system analysis and make conclusions about abc signals and behavior.

Altogether, the contributions in this thesis advance our understanding of modern power systems and provide a pathway for future work. Some examples of alternate directions for future exploration include: a grid-forming load concept to further enhance grid stability, using

the abc/dq signal relationships to understand how grid parameters influence abc frequencies, and using dq analysis to study subsynchronous oscillations.

Bibliography

[1] Carolina Albea et al. "Hybrid control scheme for a half-bridge inverter". In: *IFAC-PapersOnLine* 50.1 (2017), pp. 9336–9341.

[2] Catalin Arghir, Taouba Jouini, and Florian Dörfler. "Grid-forming control for power converters based on matching of synchronous machines". In: *Automatica* 95 (2018), pp. 273–282.

[3] Hans-Peter Beck and Ralf Hesse. "Virtual synchronous machine". In: *2007 9th International Conference on Electrical Power Quality and Utilisation*. IEEE. 2007, pp. 1–6.

[4] Jef Beerten, Salvatore D'Arco, and Jon Are Suul. "Frequency-dependent cable modelling for small-signal stability analysis of VSC-HVDC systems". en. In: *IET Generation, Transmission & Distribution* 10.6 (Apr. 2016), pp. 1370–1381. ISSN: 1751-8695, 1751-8695. DOI: 10.1049/iet-gtd.2015.0868.

[5] JP Bérard. *IEEE 9 Bus System Example*. OPAL-RT, 2017.

[6] G Bilicic and S Scroggins. *LAZARDS LCOE+ (April 2023)*. 2024.

[7] Francesco Borrelli, Alberto Bemporad, and Manfred Morari. *Predictive control for linear and hybrid systems*. Cambridge University Press, 2017.

[8] Jean Buisson, Pierre-Yves Richard, and Hervé Cormerais. "On the stabilisation of switching electrical power converters". In: *International Workshop on Hybrid Systems: Computation and Control*. Springer. 2005, pp. 184–197.

[9] Frank M Callier and Charles A Desoer. *Linear system theory*. Springer Science & Business Media, 2012, pp. 186–188.

[10] Gabriel E Colon-Reyes et al. "Transmission line dynamics on inverter-dominated grids: analysis and simulations". In: *arXiv preprint arXiv:2310.08553* (2023).

[11] C. Concordia and S. Ihara. "Load Representation in Power System Stability Studies". In: *IEEE Transactions on Power Apparatus and Systems* PAS-101.4 (Apr. 1982). Conference Name: IEEE Transactions on Power Apparatus and Systems, pp. 969–977. ISSN: 0018-9510. DOI: 10.1109/TPAS.1982.317163. URL: https://ieeexplore.ieee.org/document/4111416 (visited on 03/17/2024).

[12] S. D'Arco, J. Beerten, and J.A. Suul. "Cable Model Order Reduction for HVDC Systems Interoperability Analysis". en. In: *11th IET International Conference on AC and DC Power Transmission*. Birmingham, UK: Institution of Engineering and Technology, 2015, 026 (10 .)–026 (10 .) ISBN: 978-1-84919-982-7. DOI: 10.1049/cp.2015.0039. URL: https://digital-library.theiet.org/content/conferences/10.1049/cp.2015.0039.

[13] Salvatore D'Arco, Jon Are Suul, and Jef Beerten. "Configuration and Model Order Selection of Frequency-Dependent π Models for Representing DC Cables in Small-Signal Eigenvalue Analysis of HVDC Transmission Systems". In: *IEEE Journal of Emerging and Selected Topics in Power Electronics* 9.2 (Apr. 2021), pp. 2410–2426. ISSN: 2168-6777, 2168-6785. DOI: 10.1109/JESTPE.2020.2976046.

[14] Salvatore D'Arco, Jon Are Suul, and Jef Beerten. "Time-Invariant State-Space model of an AC Cable by *dq*-representation of Frequency-Dependent π-sections". In: *2019 IEEE PES Innovative Smart Grid Technologies Europe (ISGT-Europe)*. Bucharest, Romania: IEEE, Sept. 2019, pp. 1–5. ISBN: 978-1-5386-8218-0. DOI: 10.1109/ISGTEurope.2019.8905577. URL: https://ieeexplore.ieee.org/document/8905577/.

[15] Salvatore D'Arco, Jon Are Suul, and Olav B Fosso. "A Virtual Synchronous Machine implementation for distributed control of power converters in SmartGrids". In: *Electric Power Systems Research* 122 (2015), pp. 180–197.

[16] Rebecca Lindsey Dahlman and LuAnn. *Climate change: Global temperature*. Jan. 2024. URL: https://www.climate.gov/news-features/understanding-climate/climate-change-global-temperature.

[17] H. Dommel. "Overhead Line Parameters From Handbook Formulas And Computer Programs". In: *IEEE Transactions on Power Apparatus and Systems* PAS-104.2 (Feb. 1985), pp. 366–372. ISSN: 0018-9510. DOI: 10.1109/TPAS.1985.319051.

[18] *EPRI, NREL, and the University of Washington to Advance Electric Grid Decarbonization*. https://www.energy.gov/eere/solar/solar-energy-technologies-office-fiscal-year-2021-systems-integration-and-hardware. Accessed: 2022-02-07.

[19] *Expert Group Interaction Studies and Simulation Models (EG-ISSM)*. Tech. rep. Grid Connection European Stakeholder Committee, 2021.

[20] GE Vernova. *PSLF*. Jan. 21, 2025. URL: https://www.gevernova.com/consulting/training/pslf.

[21] Dominic Gros et al. "The Effect of Transmission-Line Dynamics on Grid-Forming Dispatchable Virtual Oscillator Control". In: *IEEE Transactions on Control of Network Systems* 6.3 (Sept. 2019), pp. 1148–1160. ISSN: 2325-5870, 2372-2533. DOI: 10.1109/TCNS.2019.2921347.

[22] Bjorn Gustavsen and Adam Semlyen. "Rational approximation of frequency domain responses by vector fitting". In: *IEEE Transactions on power delivery* 14.3 (1999), pp. 1052–1061.

[23] Nikos Hatziargyriou et al. "Stability definitions and characterization of dynamic behavior in systems with high penetration of power electronic interfaced technologies". In: *IEEE Transactions on Power Systems* (2020).

[24] Rodrigo Henriquez-Auba, Jose Daniel Lara, and Duncan S Callaway. "Small-Signal Stability Impacts of Load and Network Dynamics on Grid-Forming Inverters". In: *2024 IEEE Power & Energy Society Innovative Smart Grid Technologies Conference (ISGT)*. IEEE. 2024, pp. 1–5.

[25] Rodrigo Henriquez-Auba et al. "Grid forming inverter small signal stability: Examining role of line and voltage dynamics". In: *IECON 2020 the 46th annual conference of the IEEE industrial electronics society*. IEEE. 2020, pp. 4063–4068.

[26] Patricia Hidalgo-Gonzalez et al. "Frequency regulation in hybrid power dynamics with variable and low inertia due to renewable energy". In: *2018 IEEE Conference on Decision and Control (CDC)*. IEEE. 2018, pp. 1592–1597.

[27] David J Hill. "Nonlinear dynamic load models with recovery for voltage stability studies". In: *IEEE transactions on power systems* 8.1 (1993), pp. 166–176.

[28] Ian A Hiskens. "Power system modeling for inverse problems". In: *IEEE Transactions on Circuits and Systems I: Regular Papers* 51.3 (2004), pp. 539–551.

[29] Ian A. Hiskens. "Significance of Load Modelling in Power System Dynamics". In: *X SYMPOSIUM OF SPECIALISTS IN ELECTRIC OPERATIONAL AND EXPANSION PLANNING* (2006).

[30] "IEEE Guide for Load Modeling and Simulations for Power Systems". In: *IEEE Std 2781-2022* (Sept. 2022). Conference Name: IEEE Std 2781-2022, pp. 1–88. DOI: 10.1109/IEEESTD.2022.9905546. URL: https://ieeexplore.ieee.org/document/9905546 (visited on 03/17/2024).

[31] Brian B Johnson et al. "Synchronization of parallel single-phase inverters with virtual oscillator control". In: *IEEE Transactions on Power Electronics* 29.11 (2013), pp. 6124–6138.

[32] Rick Wallace Kenyon et al. "Open-source PSCAD grid-following and grid-forming inverters and a benchmark for zero-inertia power system simulations". In: *2021 IEEE Kansas Power and Energy Conference (KPEC)*. IEEE. 2021, pp. 1–6.

[33] Rick Wallace Kenyon et al. "Validation of maui PSCAD model: Motivation, methodology, and lessons learned". In: *2020 52nd North American Power Symposium (NAPS)*. IEEE. 2021, pp. 1–6.

[34] Hassan K Khalil. *Nonlinear systems; 3rd ed.* The book can be consulted by contacting: PH-AID: Wallet, Lionel. Upper Saddle River, NJ: Prentice-Hall, 2002. URL: https://cds.cern.ch/record/1173048.

[35] Hasan Komurcugil et al. "Sliding mode control: Overview of its applications in power converters". In: *IEEE Industrial Electronics Magazine* 15.1 (2020), pp. 40–49.

[36] Hasan Komurcugil et al. "Sliding-Mode Control for Single-Phase Grid-Connected LCL-Filtered VSI With Double-Band Hysteresis Scheme". In: *IEEE Transactions on Industrial Electronics* 63.2 (2015), pp. 864–873.

[37] Dmitry Kosterev et al. "Load modeling in power system studies: WECC progress update". In: *2008 IEEE Power and Energy Society General Meeting-Conversion and Delivery of Electrical Energy in the 21st Century*. IEEE. 2008, pp. 1–8.

[38] Ruth Kravis, Gabriel Colon-Reyes, and Duncan Callaway. "Small-signal stability in inverter-dominated grids: exploring the role of gains, line dynamics, and operating conditions". In: *arXiv preprint arXiv:2311.12152* (2023).

[39] Ruth Kravis, Gabriel E Colón-Reyes, and Duncan S Callaway. "Small-signal stability in inverter-dominated grids: exploring the role of gains, line dynamics, and operating conditions". In: *2024 IEEE Power & Energy Society General Meeting (PESGM)*. IEEE. 2024, pp. 1–5.

[40] Prabha S Kundur, Neal J Balu, and Mark G Lauby. "Power system dynamics and stability". In: *Power system stability and control* 3 (2017), pp. 700–701.

[41] Jose Daniel Lara et al. "PowerSimulationsDynamics. jl–An Open Source Modeling Package for Modern Power Systems with Inverter-Based Resources". In: *arXiv preprint arXiv:2308.02921* (2023).

[42] Jose Daniel Lara et al. *PowerSimulationsDynamics.jl – An Open Source Modeling Package for Modern Power Systems with Inverter-Based Resources*. 2023. arXiv: 2308.02921 [eess.SY].

[43] Jose Daniel Lara et al. "Revisiting Power Systems Time-domain Simulation Methods and Models". In: *IEEE Transactions on Power Systems* (2023), pp. 1–16. DOI: 10.1109/TPWRS.2023.3303291.

[44] Daniel Liberzon. *Switching in systems and control*. Vol. 190. Springer, 2003.

[45] Yashen Lin et al. *Research roadmap on grid-forming inverters*. Tech. rep. National Renewable Energy Lab. (NREL), Golden, CO (United States), 2020.

[46] K. W. Louie, J. R. Marti, and H. W. Dommel. "Aggregation of Induction Motors in a Power System Based on Some Special Operating Conditions". In: *2007 Canadian Conference on Electrical and Computer Engineering*. 2007, pp. 1429–1432. DOI: 10.1109/CCECE.2007.359.

[47] Jan Machowski et al. *Power system dynamics: stability and control*. John Wiley & Sons, 2020.

[48] Rohan Madnani and Mahesh K Mishra. "A visual understanding of electrical transformations and generalized abc to $\alpha\beta 0$ and dq0 transformation". In: *International Journal of Circuit Theory and Applications* 51.2 (2023), pp. 963–978.

[49] Manitoba Hybro Internation Ltd. *PSCAD*. Jan. 21, 2025. URL: https://www.pscad.com/.

[50] Uros Markovic et al. "Understanding small-signal stability of low-inertia systems". In: *IEEE Transactions on Power Systems* 36.5 (2021), pp. 3997–4017.

[51] Federico Milano. *Power System Modelling and Scripting*. en. Vol. 0. Power Systems. Berlin, Heidelberg: Springer Berlin Heidelberg, 2010. ISBN: 978-3-642-13668-9. DOI: 10.1007/978-3-642-13669-6. URL: http://link.springer.com/10.1007/978-3-642-13669-6.

[52] Federico Milano. *Power system modelling and scripting*. Springer Science & Business Media, 2010.

[53] Federico Milano et al. "Foundations and challenges of low-inertia systems". In: *2018 power systems computation conference (PSCC)*. IEEE. 2018, pp. 1–25.

[54] Jovica V. Milanovic et al. "International Industry Practice on Power System Load Modeling". en. In: *IEEE Transactions on Power Systems* 28.3 (Aug. 2013), pp. 3038–3046. ISSN: 0885-8950, 1558-0679. DOI: 10.1109/TPWRS.2012.2231969.

[55] Parag Mitra et al. "Modeling the aggregated response of variable frequency drives (VFDs) for power system dynamic studies". In: *IEEE Transactions on Power Systems* 35.4 (2020), pp. 2631–2641.

[56] Atef Morched, Bjorn Gustavsen, and Manoocher Tartibi. "A universal model for accurate calculation of electromagnetic transients on overhead lines and underground cables". In: *IEEE Transactions on Power Delivery* 14.3 (1999), pp. 1032–1038.

[57] Colm J O'Rourke et al. "A geometric interpretation of reference frames and transformations: dq0, clarke, and park". In: *IEEE Transactions on Energy Conversion* 34.4 (2019), pp. 2070–2083.

[58] Panteleimon Papamanolis et al. "Minimum loss operation and optimal design of high-frequency inductors for defined core and litz wire". In: *IEEE Open Journal of Power Electronics* 1 (2020), pp. 469–487.

[59] Gabriel E Colón Reyes et al. "Effects of Dynamic Power Electronic Load Models on Power Systems Analysis Using ZIP-E Loads". In: *2024 56th North American Power Symposium (NAPS)*. IEEE. 2024, pp. 1–6.

[60] Shankar Sastry. *Nonlinear systems: analysis, stability, and control*. Springer Science & Business Media, 2013, pp. 188–191.

[61] Matthew Senesky, Gabriel Eirea, and T John Koo. "Hybrid modelling and control of power electronics". In: *International Workshop on Hybrid Systems: Computation and Control*. Springer. 2003, pp. 450–465.

[62] Siemens. *PSS/E*. Jan. 21, 2025. URL: https://www.siemens.com/global/en/products/energy/grid-software/planning/pss-software/pss-e.html.

[63] Yue Song, David Hill, and Tao Liu. "Small-disturbance angle stability analysis of microgrids: A graph theory viewpoint". In: Sept. 2015. DOI: 10.1109/CCA.2015.7320633.

[64] *The MIGRATE Project*. https://www.h2020-migrate.eu/. Accessed: 2022-02-07.

[65] Xiongfei Wang et al. "Grid-synchronization stability of converter-based resources—An overview". In: *IEEE Open Journal of Industry Applications* 1 (2020), pp. 115–134.

[66] Dongsheng Yang and Xiongfei Wang. "Unified modular state-space modeling of grid-connected voltage-source converters". In: *IEEE Transactions on Power Electronics* 35.9 (2020), pp. 9700–9715.

[67] Amirnaser Yazdani and Reza Iravani. *Voltage-sourced converters in power systems: modeling, control, and applications*. John Wiley & Sons, 2010.